On the mitigation of landing gear noise using a solid fairing and a dense wire mesh

Aerospace Science and Technology 153 (2024) 109465

Contents lists available at ScienceDirect

Aerospace Science and Technology

journal homepage: www.elsevier.com/locate/aescte

On the mitigation of landing gear noise using a solid fairing and a dense wire mesh

Shuai Li [a,*], Lars Davidson [a], Shia-Hui Peng [a], Alejandro Rubio Carpio [b], Daniele Ragni [b], Francesco Avallone [c], Alexandros Koutsoukos [b]

[a] Department of Mechanics and Maritime Sciences, Chalmers University of Technology, SE-412 96 Gothenburg, Sweden
[b] Faculty of Aerospace Engineering, Delft University of Technology, Kluyverweg 1, 2629 HS Delft, the Netherlands
[c] Department of Mechanical and Aerospace Engineering, Politecnico di Torino, Corso Duca degli Abruzzi 24, 10122, Torino, Italy

ARTICLE INFO

Communicated by Damiano Casalino

Keywords:
Aeroacoustics
Landing gear noise
Noise mitigation
Wire mesh
Add-on fairings

ABSTRACT

A solid fairing and a wire-mesh fairing consisting of very fine wires and pores are numerically and experimentally investigated for the mitigation of landing gear noise. A slightly modified LAGOON landing gear and two configurations, one equipped with a solid fairing and the other with a wire-mesh fairing, are numerically simulated using the Improved Delayed Detached-Eddy Simulation (IDDES) in combination with the Ffowcs Williams and Hawkings (FW-H) analogy. Instead of resolving the detailed flow features through the wire mesh, a recently proposed numerical model is used to represent the effect of the wire-mesh fairing. The simulated flow fields and the far-field noise spectra are validated against the experiments conducted in an anechoic wind tunnel. The superiority of the recently proposed wire-mesh model over a classical wire-mesh model in modelling both the aerodynamic and aeroacoustic effects of the wire mesh is demonstrated. Results also show that the dense wire-mesh fairing functions very similarly to the solid fairing and that significant noise can be reduced through the installation of a solid fairing or a wire-mesh fairing upstream of the landing gears. For the baseline landing gear, the torque link and the brakes are identified noise sources. With the aerodynamic penalty of a 50% increase in drag, both fairings mitigate the pressure fluctuation on the torque link and brakes, resulting in the reduction of surface noise sources. The noise directivity shows that a solid fairing or a dense wire-mesh fairing contributes to a noise reduction of 4-6 dB in all radial directions. The findings in this study pave the way for the low-noise design of aircraft landing gears.

1. Introduction

Aircraft noise has become an increasingly pressing topic of concern in aviation design due to its detrimental impact on people living in the vicinity of airports [1,2]. Aircraft noise results from a combination of engine noise generated by the fan and the jet, and airframe noise generated by landing gear (LG) systems and high-lift devices (HLD). With the advent of quieter, ultra-high-bypass-ratio engines, airframe noise has emerged as an important contributor, particularly during approach and landing phases [3]. For long-range aircrafts, the LG noise tends to be the dominant contributor to the airframe noise [4,5]. The LG noise is mainly generated by (i) flow separation off different individual structural components (wheels, brakes, struts, axles and torque links, etc.) and (ii) interaction of turbulent wakes from upstream components with downstream structural components [6]. Due to the complexity of noise-generation mechanisms, the mitigation of LG noise is a challenging task and has attracted intensive research efforts.

Over the past two decades, fairings have been demonstrated to be a good technological solution for LG noise reduction. Solid fairings were first deployed for LG noise reduction. Wind-tunnel experiments were conducted to study the effect of solid fairings on noise reduction in European Union (EU) projects, among others, the RAIN (Reduction of Airframe and Installation Noise) [7], the SILENCER (Significantly Lower Community Exposure to Aircraft Noise) [8], the TIMPAN (Technologies to Improve Airframe Noise) [9], the QTD 2 (Quiet Technology Demonstrator 2) [10] and the ALLEGRA (Advanced Low Noise Landing Gear for Regional Aircraft) projects [11,12]. In these projects, the function of solid fairings in noise reduction has been well demonstrated. How-

* Corresponding author.
E-mail address: shuai.li@chalmers.se (S. Li).

https://doi.org/10.1016/j.ast.2024.109465
Received 1 December 2023; Received in revised form 19 July 2024; Accepted 5 August 2024
Available online 8 August 2024

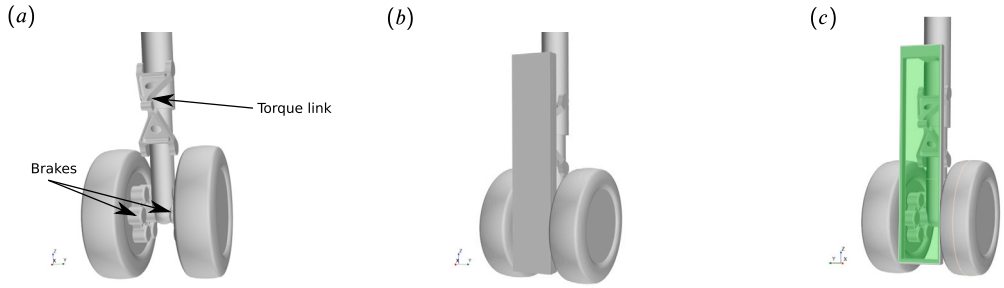

Fig. 1. The slightly modified LAGOON landing gear equipped with brakes and a torque link: (a) Baseline case; (b) controlled case with a solid fairing; and (c) controlled case with a DLR wire mesh.

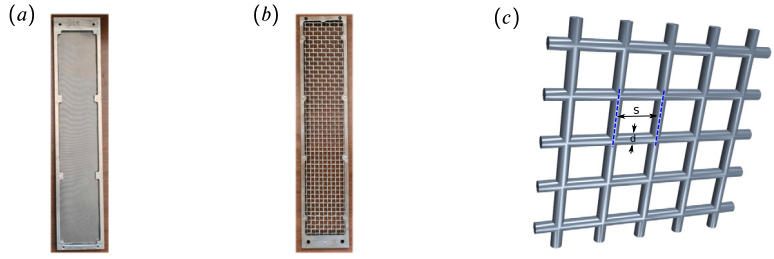

Fig. 2. Two different types of wire meshes: (a) The fine DLR wire mesh; (b) the coarse ONERA wire mesh; and (c) the close-up view of a wire mesh [33].

ever, a major drawback of solid fairings is that the flow can be deflected to adjacent and downstream components, enhancing the interaction between the turbulent wake and downstream components [13]. Besides, compared to porous fairings, flow velocities towards the fairing sides are more significant [13], leading to larger-scale flow separation and higher aerodynamic drag.

Alternatively, porous wire meshes (WM) have been investigated within the TIMPAN [14,15], the ALLEGRA [16,17], and the IMAGE (Innovative Methodologies and technologies for reducing Aircraft noise Generation and Emission) projects [18–21]. Compared to solid fairings, a key advantage of wire-mesh fairings is that the flow is not deflected towards the fairing sides due to the mass flux through the pores, potentially leading to less aerodynamic drag. Besides, wire-mesh fairings have other benefits such as lighter weight and higher visibility. The mechanism of bluff-body noise reduction using wire meshes has been intensively explored in the aforementioned projects. As summarized by Zhao et al. [13], this is associated with three possible aspects, all interfering with bluff-body aerodynamics. First, wire meshes dampen local impinging flow velocities; second, wire meshes may break up the incoming flow into small vortices so that spanwise coherent vortices shedding from the downstream bluff body are altered; third, wire meshes may shift the vortex shedding away from bluff-body surfaces, consequently reducing the acoustic radiation efficiency. The work reported in this paper has been carried out within the framework of the ongoing EU H2020 INVENTOR (Innovative Design of Installed Airframe Components for Aircraft Noise Reduction) project [22–24].

In the INVENTOR project, a slightly modified version of the original LAGOON landing gear is used together with a torque link (TL) and two brakes, see Fig. 1(a). This LG configuration is obtained by closing the inner rim cavities of the original LAGOON landing gear in order to avoid the Rossiter instabilities [25]. Several previous numerical studies of the LAGOON landing gear have been presented in the AIAA Benchmark problems for Airframe Noise Computations (BANC) - III workshop [5,25–32]. In these and many other previous studies, the noise generation mechanism of the LAGOON landing gear has been studied. A major noise source is generated by the LG wheels and struts which cause large-scale flow separation and vortex shedding. Another noise source is found to be associated with the onset of cavity modes in the two facing rim cavities of the LAGOON LG [25]. Nevertheless, no systematic investigation on the noise mitigation of the LAGOON LG has been reported. Given the aforementioned advantages and disadvantages of solid and wire-mesh fairings in LG noise mitigation, a systematic study of the aerodynamic and aeroacoustic performances of a porous wire-mesh fairing versus a solid fairing is imminently favored, particularly considering that the use of add-on fairings for LG noise abatement has a high technology readiness level (TRL) and is suitable for flight testing and commercial implementation soon in the 2020s [12].

In the present study, we investigate the reduction of the slightly modified LAGOON landing gear noise by performing wind-tunnel experiments and IDDES of three LG cases, i.e., a baseline case, a controlled case with a solid fairing, and a controlled case with a novel dense wire mesh consisting of very fine wires and pores, see Fig. 1. This wire mesh was fabricated by the German Aerospace Center (DLR) and is hereinafter called the DLR wire mesh (DLRWM). Fig. 2 shows the fine DLR wire mesh, the coarse ONERA wire mesh and a sketch of an isolated wire mesh. Due to the very fine wires and pores of the DLR wire mesh, detailed meshing of the DLR wire mesh is not practical since it would result in a large number of computational cells. A numerical wire-mesh model is thus required. Recently, Li et al. [33] proposed a wire-mesh model to represent the effect of the DLR wire mesh in numerical simulations. This model overcomes the limitation of the existing wire-mesh models [18,19] and has been shown to perform better in modelling the wire mesh consisting of very fine wires and pores, as evidenced by the numerical modelling of the DLR wire mesh in channel flow simulations [33]. In the present study, we also evaluate both the aerodynamic and aeroacoustic prediction accuracies of this model when applied in external flow simulations (i.e. flows past the LAGOON-like landing gear).

The paper is structured as follows: §2 is devoted to a description of the experimental set-up, numerical method, computational meshes and numerical set-up for the simulations of landing gears. The details of the wire-mesh models for the controlled LG with the DLR wire mesh are described in §3. Flow and acoustic results of the simulations are presented in §4. Finally, concluding remarks are summarized in §5.

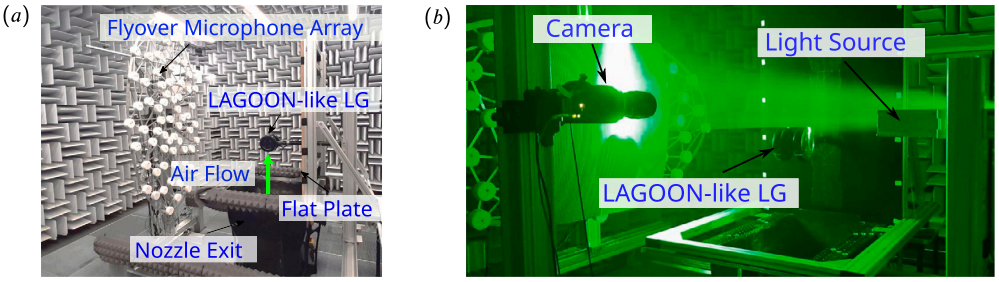

Fig. 3. Experimental setup in the anechoic A-Tunnel: (a) Acoustic measurement; and (b) PIV measurement [34].

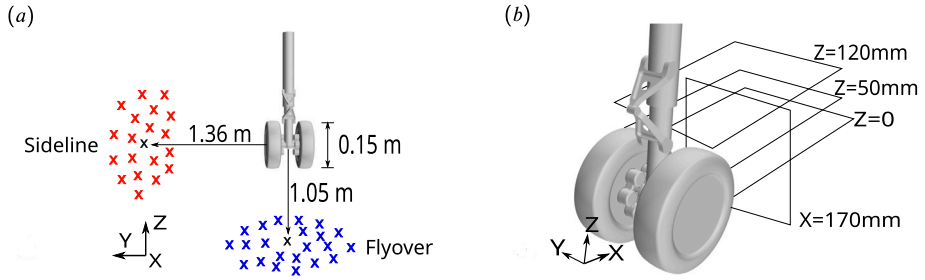

Fig. 4. Microphone and PIV measurements: (a) Sideline (in red) and flyover (in blue) microphone measurement configurations. Each microphone array consists of 64 microphones with the center microphone highlighted in black color; and (b) a sketch of four planes downstream of a landing gear where flow fields are measured using PIV. (For interpretation of the colors in the figure(s), the reader is referred to the web version of this article.)

2. Methodologies

2.1. Experimental set-up

The measured flow statistics and acoustic spectra of the LAGOON-like landing gear used for the validation of the present numerical simulations are obtained in the A-Tunnel of the Delft University of Technology [22–24,34]. The A-Tunnel is an open-jet, closed-circuit, vertical wind tunnel. The open-jet test section of the wind tunnel is located inside an anechoic room with dimensions $6.4 \times 6.4 \times 3.2\,\mathrm{m}^3$. The walls and ceiling of the anechoic room are covered with wedges made of Flamex acoustic absorbing foam in order to avoid unwanted sound reflections. The vertical nozzle has a rectangular exit with dimensions of $400 \times 700\,\mathrm{mm}^2$, see Fig. 3. Fig. 4(a) shows two microphone measurement configurations. A single microphone array is deployed in these two measurement configurations: flyover, with the array placed at the bottom of the LG, and sideline, placed laterally. The microphone array consists of 64 GRAS 40PH analog free-field microphones with integrated constant current power amplifiers. The 64 microphones are distributed over a planar ellipse with a major-to-minor axis ratio of 2 and a major effective diameter of 2 m [22]. The center microphone of the flyover configuration is located at $(X, Y, Z) = (0.22, -0.02, -1.05)$ m and that of the sideline configuration is located at $(0.22, 1.36, 0)$ m, where X, Y, Z are the streamwise, lateral and vertical direction, respectively. The origin of the coordinate system is located at the intersection between the axis of the LG axle and the axis of the rod connecting the two wheels. The diameter of the LG wheels is $d_w = 150$ mm. For all the acoustic measurements conducted in the present study, a recording time of 20 seconds and a sampling frequency of 51.2 kHz are adopted. The spectra of the acoustic signals are obtained using Welch's method [35] with a Hanning windowing function and 50% data overlap. The one-third octave bin-averaging technique is applied to smooth the sound spectra.

The A-Tunnel facility is mainly meant for aeroacoustic measurements, but it is also equipped with flow measurement techniques, such as a Particle Image Velocimetry (PIV) system (see Fig. 3(b)). Planar PIV measurements using a LaVision Imager sCMOS CLHS camera at a frame rate of 15 Hz are conducted to measure the flow velocities in the LG wake region, i.e. on a vertical plane $X = 170$ mm and three horizontal planes $Z = 0$, $Z = 50$ mm and $Z = 120$ mm with a field of view (FOV) of $180 \times 240\,\mathrm{mm}^2$ (see Fig. 4(b)). The resolution of the FOV is 24×24 pixels with a vector spacing of 0.6 mm. These flow-field measurements at 35 m/s will be used to validate the predicted flow field in the present numerical simulations. For more details on the experiments, see Refs. [22–24,34,36].

2.2. Numerical method

The simulations are performed using a commercial finite-volume solver, STAR-CCM+, version 2021.1 [37]. The compressible Navier-Stokes equations are solved in a coupled manner. Convective fluxes are approximated using the bounded central difference scheme (a hybrid of second-order upwind and central difference schemes). For the diffusive flux, a second-order accurate scheme is used for the interior grid cells. An implicit, 2nd-order, three-level Euler scheme is used for the time integration in transient simulations. For details on STAR-CCM+, the readers may refer to the User Guide for the detailed numerical algorithms [38]. The numerical approaches used in the present study are briefly introduced below.

The turbulent flow past the landing gears is computed using the IDDES method based on the SST $k-\omega$ model [39]. The detached eddy simulation (DES) method is considered the best trade-off between the computational cost and prediction accuracy in resolving engineering flows. In the near-wall region, the flow is predicted by solving the Reynolds-Averaged Navier-Stokes (RANS) equations. Meanwhile, the flow in the region away from the walls is resolved using Large Eddy Simulation (LES). Delayed Detached Eddy Simulation (DDES), an improved version of the original DES method, lessens the impact of grid-induced separation caused by inappropriate activation of the LES mode in the near-wall region. The IDDES method, a hybrid of DDES and the wall-modelled LES, introduces modifications in the length scale of the dissipation rate in the Turbulent Kinetic Energy (TKE) transport equation of the SST $k-\omega$ model [39]. The grid filter in IDDES, as a function of the grid size and the wall distance, is expressed as

$$\Delta_{IDDES} = \min(\max(0.15 d_{wall}, 0.15\Delta_{max}, \Delta_{wn}), \Delta_{max}), \quad (1)$$

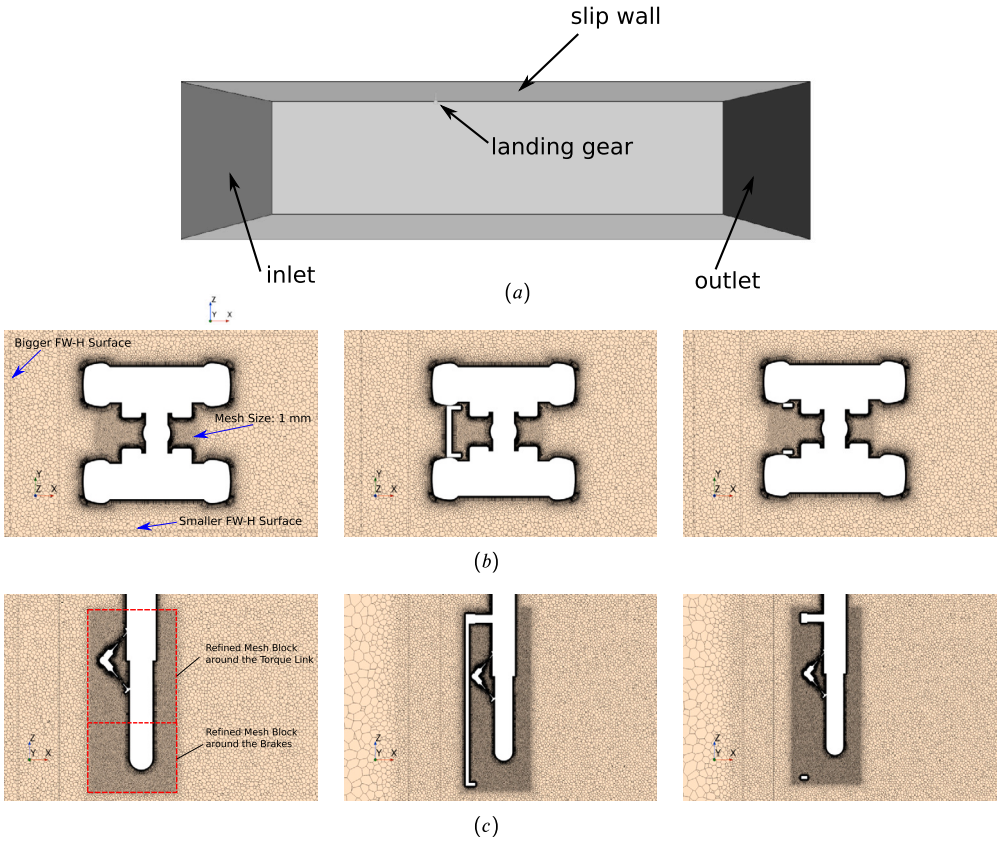

Fig. 5. Computational domain and meshes: (*a*) computational domain with boundary conditions; (*b*) mesh on plane $Z = 0$; and (*c*) mesh on plane $Y = 0$. For (*b*) and (*c*), from left to right: Baseline case, controlled case with a solid fairing, and controlled case with the DLR wire-mesh fairing.

where d_{wall} is the wall distance, Δ_{max} is the largest grid spacing in all three directions, and Δ_{wn} is the grid spacing in the wall-normal direction.

The IDDES length scale can be expressed as a combination of the RANS and LES length scales, as follows

$$l_{IDDES} = \tilde{f}_d(1 + f_e)l_{RANS} + (1 - \tilde{f}_d)l_{LES}, \tag{2}$$

where $\tilde{f}_d$ is a delaying function, f_e is an evaluating function, l_{RANS} is the RANS length scale and l_{LES} is the LES length scale. The RANS and LES length scales can be respectively obtained as

$$l_{RANS} = \sqrt{k}/(0.09\omega) \tag{3}$$

where k is the turbulent kinetic energy and ω is the specific dissipation rate, and

$$l_{LES} = C_{DES}\Delta_{IDDES}, \tag{4}$$

where $C_{DES} = 0.78$ is a DES model coefficient and Δ_{IDDES} is the mesh length scale [38].

The far-field noise is predicted using the FW-H analogy with a permeable integral surface. The FW-H equation is solved in time domain using the Farassat's formulation 1A [40–42]. The readers may refer to the Appendix for more details.

2.3. Computational meshes and simulation set-up

The dimensions of the computational domain in the streamwise, vertical and spanwise directions are $130d_w$, $65d_w$ and $32.5d_w$, respectively. Fig. 5(a) shows the computational domain and the boundary conditions. Besides the inlet, outlet and slip wall, the other three boundaries are free-stream boundaries. A no-slip wall boundary condition is applied on the LG surfaces. In the simulations, the LG axle is attached to a slip wall in order to mimic the flat plate (see Fig. 3(a)) in the wind-tunnel measurements. In the present study, a baseline case and two controlled cases, one with a solid fairing and the other with the DLR wire mesh, are simulated to study the noise-reduction performances of solid and porous fairings (see Fig. 1). The detailed flow features past the baseline case and the controlled case with a solid fairing are resolved with refined grids. For the controlled case with the DLR wire mesh, instead of resolving the detailed flow through the DLR wire mesh, a numerical model is used to represent the wire-mesh effect (see Section 3). This is because the opening of the DLR wire mesh is much smaller compared to the LG geometry. The detailed meshing of the geometry and the wire mesh is impractical since it will result in a very large amount of computational cells.

The computational mesh is generated by the STAR-CCM+ built-in mesh generator. The Polyhedral Mesher is adopted to generate polyhedral cells in the flow field. In the vicinity of solid walls, the Advancing Layer Mesher is used to generate prism layers. The first cells from the solid walls typically have y^+ values of less than 1. However, a small number of cells near the sharp edges exhibit y^+ values slightly above 1, as shown in Fig. 6. Table 1 shows six computational cases of the LAGOON-like landing gear. Cases 1-3 are dedicated to the baseline LG simulations and are also used for the grid sensitivity study. Case 4 is used for the controlled LG with a solid fairing. Cases 5-6 simulate the controlled LG with the DLR wire mesh which is represented by two different wire-mesh models. In all six cases, the polyhedral mesh is refined around the brakes and the torque link, resulting in refined mesh blocks around the brakes and the torque link (see Fig. 5(b) and (c)). Except for case 3, the polyhedral cell size of the refined blocks is $\Delta s/d_w = 0.0067$ (i.e. $\Delta s = 1$ mm). In the X direction, the lengths of the refined blocks around the brakes (L_X^{BK}) and the torque link (L_X^{TL}) are listed in Table 1. In the Y direction, the widths of the refined blocks around the brakes

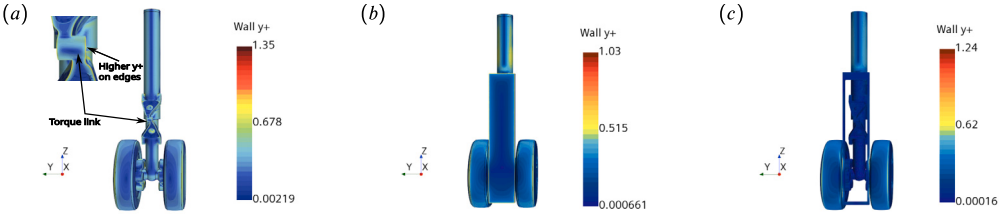

Fig. 6. The y^+ distribution on the surface of the landing gear: (*a*) Baseline configuration (case 1); (*b*) controlled configuration with a solid fairing (case 4); and (*c*) controlled configuration with the DLR wire-mesh fairing (case 6).

Table 1
Simulation cases for the baseline and controlled landing gears.

Case	L_X^{BK}/d_w [a]	$\Delta s^{BK}/d_w$ [b]	L_X^{TL}/d_w [c]	$\Delta s^{TL}/d_w$ [d]	# M. cells	Configuration	Effect of fairing
1	0.69	0.0067	0.69	0.0067	73	Baseline	No fairing
2	2.11	0.0067	2.11	0.0067	75	Baseline	No fairing
3	0.69	0.0067	0.69	0.0033	78	Baseline	No fairing
4	0.69	0.0067	0.69	0.0067	89	Solid	Resolved
5	0.75	0.0067	0.75	0.0067	87	DLRWM	Modelled (Eq. (6))
6	0.75	0.0067	0.75	0.0067	87	DLRWM	Modelled (Eq. (9))

[a] L_X^{BK} denotes the length of the refined block around the brakes in X direction.
[b] Δs^{BK} denotes the polyhedral cell size of the refined block around the brakes.
[c] L_X^{TL} denotes the length of the refined block around the torque link in X direction.
[d] Δs^{TL} denotes the polyhedral cell size of the refined block around the torque link.

and the torque link are $L_Y^{BK}/d_w = L_Y^{TL}/d_w = 0.42$. In the Z direction, for cases 1-3, the heights of the refined blocks around the brakes and the torque link are $L_Z^{BK}/d_w = 0.54$ and $L_Z^{TL}/d_w = 0.92$, respectively. For cases 4-6, due to the large spanwise length of the fairings, the corresponding heights are $L_Z^{BK}/d_w = 0.67$ and $L_Z^{TL}/d_w = 1.23$, respectively. Moreover, the mesh is refined in the wake region over a distance of $10d_w$ downstream of the landing gear and has a coarser cell size of $\Delta s/d_w = 0.025$. The total numbers of grid cells in the present simulations are shown in Table 1. Fig. 5(b) and (c) shows the mesh distribution on planes $Z = 0$ and $Y = 0$, respectively, for the baseline (Case 1) and controlled cases with a solid fairing and the DLR wire-mesh fairing.

The free-stream velocity is $U_0 = 35$ m/s with a low turbulence intensity of 0.1% and a turbulent viscosity ratio of 1.0 at the inlet boundary condition which gives the dissipation rate ω. The Reynolds number, based on the free-stream velocity and the diameter of wheels, is 350,000 approximately. A relatively small time step of $\Delta t = 1.0 \times 10^{-5}$ seconds is used to advance the simulations in time. In the present numerical simulations, we validate the predicted flow field by comparing the velocity statistics along the wake center line ($Y = 0$) and a vertical line ($X = 1.7d_w$) in the three horizontal planes $Z = 0$, $Z = 50$ mm and $Z = 120$ mm (see Fig. 4(b)). The far-field noise is computed by integrating the noise sources on a permeable integral surface according to the FW-H analogy. The integral surface is a box with the downstream end open in order to avoid the spurious noise generated by the passage of turbulent eddies through the downstream surface. In the simulations, a smaller and a bigger permeable FW-H surfaces are tested. The smaller FW-H surface encloses the region of $(-0.67 \le X/d_w \le 4, -0.67 \le Y/d_w \le 0.67, -1 \le Z/d_w \le 2.33)$, while the bigger FW-H surface encloses the region of $(-1 \le X/d_w \le 10, -1 \le Y/d_w \le 1, -1.5 \le Z/d_w \le 2.33)$. The position of the integral surfaces has been carefully selected so that it is far enough from the turbulent wake while it is still located within the refined region to ensure sufficient grid resolution. Similar noise spectra are obtained using both FW-H surfaces. For the sake of plot conciseness, only the results pertaining to the smaller FW-H surface are presented. The grid resolution here enables a cut-off frequency of approximately 20 kHz. In the simulations, the pressure signal is sampled with a frequency of 100 kHz over a duration of 0.25 seconds after the initial transient flow state.

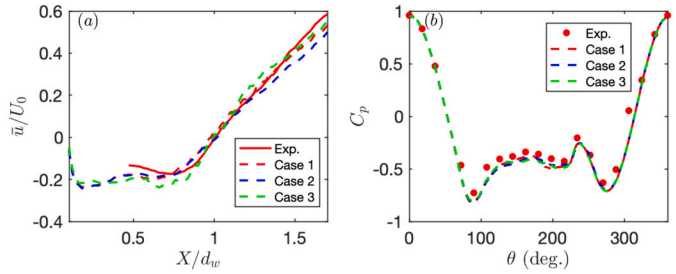

Fig. 7. Comparison of flow quantities among three different computational meshes (cases 1-3) for the baseline LG: (*a*) Mean streamwise velocity along the wake center line at Z = 0; and (*b*) pressure coefficient (C_p) on the surface of the LG rod at $Z = 50$ mm.

2.4. Grid sensitivity study

A grid sensitivity study is performed for the baseline LG with three different computational meshes. The first mesh has relatively small refined blocks around the brakes and the torque link with a cell size of $\Delta s/d_w = 0.0067$. The second mesh is made by extending the refined mesh blocks around the brakes and the torque link to $1.7d_w$ downstream the LG, leading to $2.11d_w$-long refined blocks and a total number of grid cells of 75.4 million. The third mesh is obtained by reducing the polyhedral cell size of the refined mesh block around the torque link from $\Delta s/d_w = 0.0067$ to 0.0033, leading to a total number of grid cells of 78.3 million. Fig. 7 shows a comparison of flow quantities using 3 different computational meshes for the baseline LG. The convergence of mean flow in the LG wake and pressure distribution on the LG rod demonstrates that the current mesh resolution is sufficient for the LG simulations. Hence, hereinafter, among the three baseline cases 1-3, results are presented only for case 1.

3. The wire-mesh models

3.1. The classical wire-mesh model

Similar to the modelling of other porous media [43–46], the model of a wire mesh in flows is a damping-type source term added to the momentum equations [16–21]. Within the wire-mesh region, a volume-

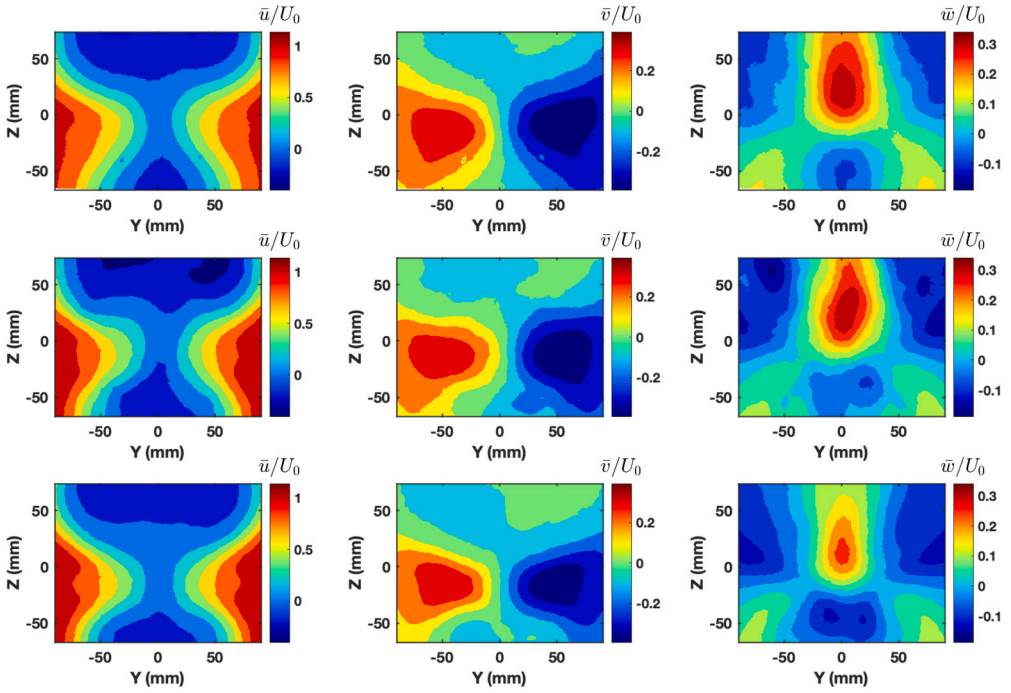

Fig. 8. Comparison of mean velocities in plane $X = 170$ mm between PIV measurement and IDDES of the DLRWM configuration. First row: PIV; second row: IDDES using wire-mesh Model II; third row: IDDES using wire-mesh Model I.

averaged source term S is added to the right-hand side (RHS) of the IDDES momentum equations, yielding the momentum equations as

$$\frac{\partial(\rho\hat{u}_i)}{\partial t} + \frac{\partial(\rho\hat{u}_i\hat{u}_j)}{\partial x_j} = -\frac{\partial\hat{p}}{\partial x_i} + \frac{\partial\hat{\sigma}_{ij}}{\partial x_j} + \frac{\partial\sigma_{ij,model}}{\partial x_j} + S_i, \tag{5}$$

where ρ is the fluid density, $\hat{u}_i$ is the components of velocity (i =1, 2, 3), $\hat{p}$ is the pressure, '^' denotes a Reynolds-averaged quantity in the RANS region and a filtered quantity in the LES region, respectively. $\hat{\sigma}_{ij}$ is the viscous stress tensor and $\sigma_{ij,model}$ is the modelled stress tensor.

If the airflow approaches the wire mesh at zero incident angle, the source term is expressed as

$$\begin{bmatrix} S_1 \\ S_2 \\ S_3 \end{bmatrix} = \begin{bmatrix} -K_0 \times 0.5\rho\,|\hat{u}|\,\hat{u}/h \\ 0 \\ 0 \end{bmatrix}, \tag{6}$$

where $\hat{u}$ here is the streamwise velocity, h is the fairing thickness and the resistance coefficient K_0 is given by an empirical formula [47]

$$K_0 = \left(0.5 + \frac{26}{Re_d}\right)\left(\frac{1-\beta^2}{\beta^2}\right), \tag{7}$$

where the porosity β is expressed as

$$\beta = (1 - d/s)^2. \tag{8}$$

The DLR wire mesh consists of wires with a diameter of $d = 0.042$ mm and a spacing between the wires of $s = 0.14$ mm, thus leading to a porosity of $\beta = 0.59$.

3.2. The improved wire-mesh model

Although the wire-mesh model in Section 3.1 has been successfully applied to model wire meshes with relatively large wires and lattices [18,19], it is also found that this model does not function well in modelling the novel DLR wire mesh with fine wires and pores [33]. To overcome this limitation, Li et al. [33] recently proposed an improved model by adding a linear term, proportional to the flow velocity, to the above source term of the momentum equations. The linear viscous resistance and nonlinear inertial resistance of porous media, related to the permeability of porous media, were experimentally studied [48–50]. The wire-mesh model of Li et al. [33] has been validated against experiments previously conducted in the Wind tunnel for AeroAcoustic Boundary Layer Including prEssure gradient eFfect (WAABLIEF) of the von Karman Institute (VKI) for Fluid Dynamics [51].

In the new wire-mesh model [33], for air flows approaching the wire mesh at zero incident angle, the source term is expressed as a combination of a linear term and a quadratic term, as follows,

$$\begin{bmatrix} S_1 \\ S_2 \\ S_3 \end{bmatrix} = \begin{bmatrix} -\mu\hat{u}/K_{perm} - K_0 \times 0.5\rho\,|\hat{u}|\,\hat{u}/h \\ 0 \\ 0 \end{bmatrix}, \tag{9}$$

where μ is the dynamical viscosity, K_{perm} is a characterization of the permeability of the wire mesh and can be determined using the pressure loss measured in a wind tunnel with the wind-tunnel cross-section fully covered by the wire mesh [33,52], and the form coefficient K_0 is given by Eq. (7). The readers may refer to Li et al. [33] for more details on this model and its validation against experimental data. It should be noted that, although the damping-type source term is added to the DES momentum equations, the wire-mesh model is applicable to other scale-resolving simulations and RANS.

To distinguish the aforementioned classical model (Eq. (6)) and the present improved model (Eq. (9)), the classical model and the improved model are denoted as 'Model I' and 'Model II', respectively.

4. Results

In this section, flow and acoustic results are presented and discussed for the baseline case, and the controlled cases with, respectively, a solid fairing and the DLR wire mesh.

4.1. Comparison of flow and acoustic predictions between both wire-mesh models

Figs. 8 and 9 compare the mean velocities and root-mean-square velocity fluctuations, respectively, between the PIV measurement [22–24,36] and IDDES of the DLRWM configuration using both wire-mesh models. Overall, the simulations align reasonably well with the experiment.

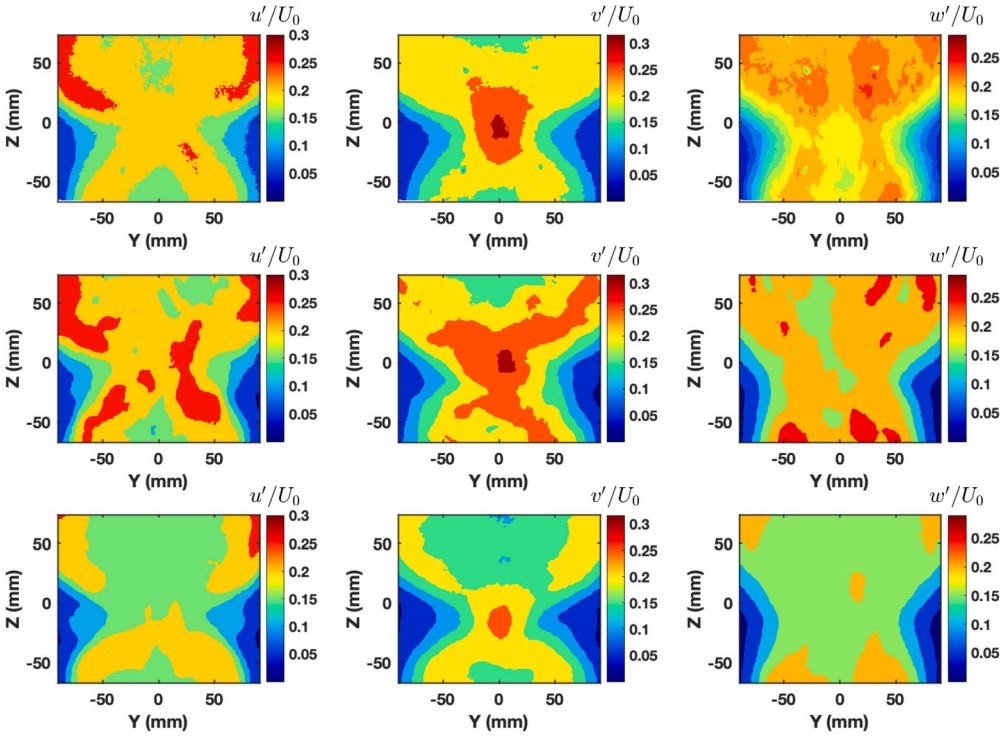

Fig. 9. Comparison of root-mean-square velocity fluctuations in plane $X = 170$ mm between PIV measurement and IDDES of the DLRWM configuration. First row: PIV; second row: IDDES using wire-mesh Model II; third row: IDDES using wire-mesh Model I.

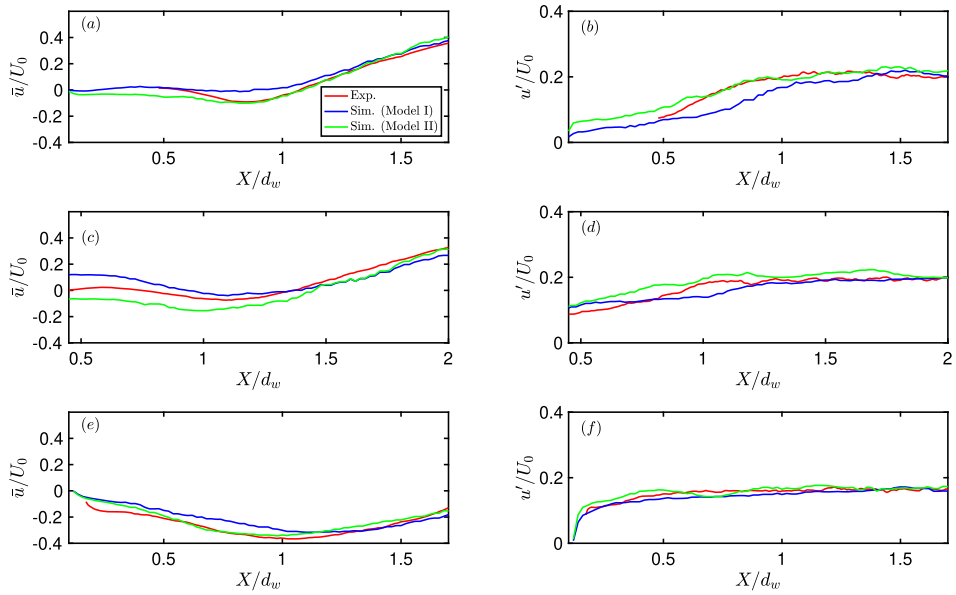

Fig. 10. Comparisons of flow statistics along the LG wake center lines between both models for the controlled case with the DLR wire-mesh fairing: (*a*) Mean streamwise velocity at $Z = 0$; (*b*) root-mean-square of streamwise velocity fluctuation at $Z = 0$; (*c*) mean streamwise velocity at $Z = 50$ mm; (*d*) root-mean-square of streamwise velocity fluctuation at $Z = 50$ mm; (*e*) mean streamwise velocity at $Z = 120$ mm; and (*f*) root-mean-square of streamwise velocity fluctuation at $Z = 120$ mm.

Both wire-mesh models produce similar results, with the contours of $\bar{w}$ and w' in model II showing slightly better agreement with the PIV measurement.

Fig. 10 shows the comparisons of the mean streamwise velocity profile and the root-mean-square of the streamwise velocity fluctuation profile along the LG wake center lines using both Model I (Eq. (6)) and Model II (Eq. (9)). At $Z = 0$, the predictions given by Model II generally agree better with the experiments. This is more noticeable at locations where there is a big discrepancy between the experimental data and the predictions given by Model I. At $Z = 50$ mm, the mean streamwise velocity profiles predicted by both models deviate from the experiment in the LG near wake (i.e. $X/d_w < 1.5$). Further downstream, Model II produces slightly better agreement with the experiment. At $Z = 50$ mm, however, Model I gives a better prediction of the root-mean-square of the streamwise velocity fluctuation. At $Z = 120$ mm, both models give comparable predictions, although better agreement in the mean streamwise velocity is observed for Model II between $0.5d_w$ and $1.0d_w$ in the wake.

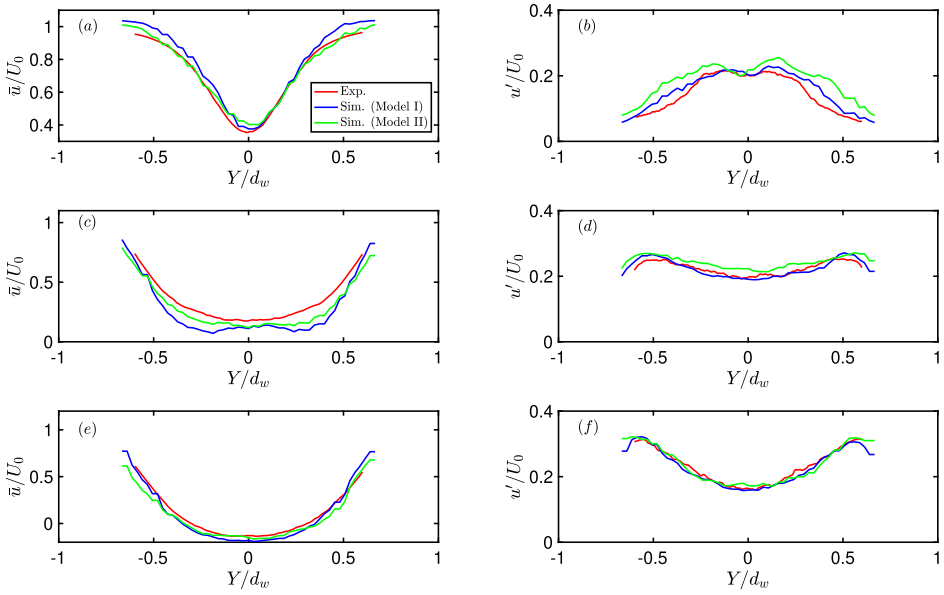

Fig. 11. Comparisons of flow statistics along the wake vertical lines at $X = 1.7d_w$ between both models for the controlled case with the DLR wire-mesh fairing: (*a*) Mean streamwise velocity at $Z = 0$; (*b*) root-mean-square of streamwise velocity fluctuation at $Z = 0$; (*c*) mean streamwise velocity at $Z = 50$ mm; (*d*) root-mean-square of streamwise velocity fluctuation at $Z = 50$ mm; (*e*) mean streamwise velocity at $Z = 120$ mm; and (*f*) root-mean-square of streamwise velocity fluctuation at $Z = 120$ mm.

Fig. 11 shows the comparisons of the mean streamwise velocity profile and the root-mean-square of the streamwise velocity fluctuation profile along the LG wake vertical lines at $X = 1.7d_w$ using both models. At $Z = 0$ and $Z = 50$ mm, overall, the mean streamwise velocity profile predicted by Model II agrees better with the experiment. Conversely, the root-mean-square of the streamwise velocity fluctuation is better predicted by Model I. Compared to Model I, Model II gives larger velocity fluctuations than Model I since Model II indeed produces a stronger vortex shedding, as also suggested by Li et al. [33]. At $Z = 120$ mm, both models give very similar predictions. In view of the effect on the prediction of mean flow (1st-order statistics) and in comparison with available experimental data, Model II shows a slightly better performance in representing the aerodynamic effect of the fine DLR wire mesh. Considering that the comparisons are made in the wake very far downstream of the DLR wire-mesh fairing, Model II is more advantageous for the very fine DLR wire mesh.

Fig. 12 shows the comparisons of the one-third octave bin-averaged sound pressure levels (SPL) at both flyover and sideline microphone arrays. For the flyover array, at the center microphone, the spectra predicted by both models agree with the experiment in the low to middle frequency range but deviate from the experiment from 3000 Hz and agree with the experiment again from 12000 Hz. Meanwhile, the average of all 64 flyover microphones shows that Model I slightly underpredicts the spectra in the low to middle frequency range while Model II gives a better prediction. For the sideline array, the under-prediction of sound spectra in the low to middle frequency range by Model I is more evident while the spectra predicted by Model II generally agree better with the experiment. Overall, all predicted spectra in Fig. 12 possess a deviation from the experiment at frequencies between 3000 Hz and 12000 Hz. This deviation may result from the insufficient accuracies in resolving the flow features at the small gaps (with a dimension of 0.5 mm) between the fairing and the LG wheels. As can be seen below in the contours of the mean streamwise velocity, the airflow passes the gaps at a velocity between $0.3U_0$ and U_0. If we take a velocity of $0.65U_0$ to estimate the Strouhal number, a noise frequency of 8000 Hz in the aforementioned frequency range corresponds to a Strouhal number of 0.18 approximately. This implies that the aforementioned deviation is likely due to the insufficient accuracies in resolving the small gaps between the fairing and the LG wheels.

It has been verified in the previous work of Li et al. [33] that Model II is able to produce better aerodynamic predictions than Model I in internal flows (i.e. channel flows). Based on the comparisons in Figs. 10 - 12, it is further shown that Model II generally performs well in both aerodynamic and aeroacoustic predictions of external flows, and is even superior to Model I in modelling the DLR wire mesh. This will also be better demonstrated by the directivity of sound pressure level in Section 4.3. Hence, hereinafter, unless otherwise noted, the baseline simulation using Model II is used for the analysis.

4.2. Comparison of the baseline and controlled cases: flow field

Figs. 13 and 14 compare contours of the mean velocities and root-mean-square velocity fluctuations in plane $X/d_w = 1.13$ between PIV measurement and IDDES of the baseline and solid-fairing configurations. The mean velocities and root-mean-square velocity fluctuations of the DLRWM configuration have been previously shown in Figs. 8 and 9, respectively. Overall, good agreement between the IDDES and PIV measurement is observed. Quantitative comparisons of the flow statistics between the IDDES and PIV measurement are presented subsequently.

Fig. 15 shows the instantaneous streamwise velocity on the isosurface of $Q_{cr} = 100\ s^{-2}$ for the baseline case and the two controlled cases. For the baseline case, the vortices downstream of the landing gear are generally finer due to the relatively small dimensions of the torque link and the LG leg. For the controlled cases, the vortices downstream of the fairings are relatively large in the presence of the fairings with a larger dimension.

Fig. 16 shows the contours of the mean streamwise velocity on three different planes in the LG wake region for the baseline and the two controlled cases. As the flow passes over the landing gears, the flow accelerates on both sides of the landing gears, forming a flow region with higher flow speeds. With the shielding of the fairings, the recirculation region of the two controlled cases is much larger than that of the baseline case at planes $Z = 50$ mm and $Z = 120$ mm. However, at $Z = 0$, it is not, because this plane passes through the horizontal rod connecting the two wheels. As a result, the shielding effect of the fairings does not make much difference at $Z = 0$. This is also the reason why the downstream wake in the two controlled cases does not become broader at plane $Z = 0$, compared to the baseline case. At $Z = 50$ mm, without fairings, the

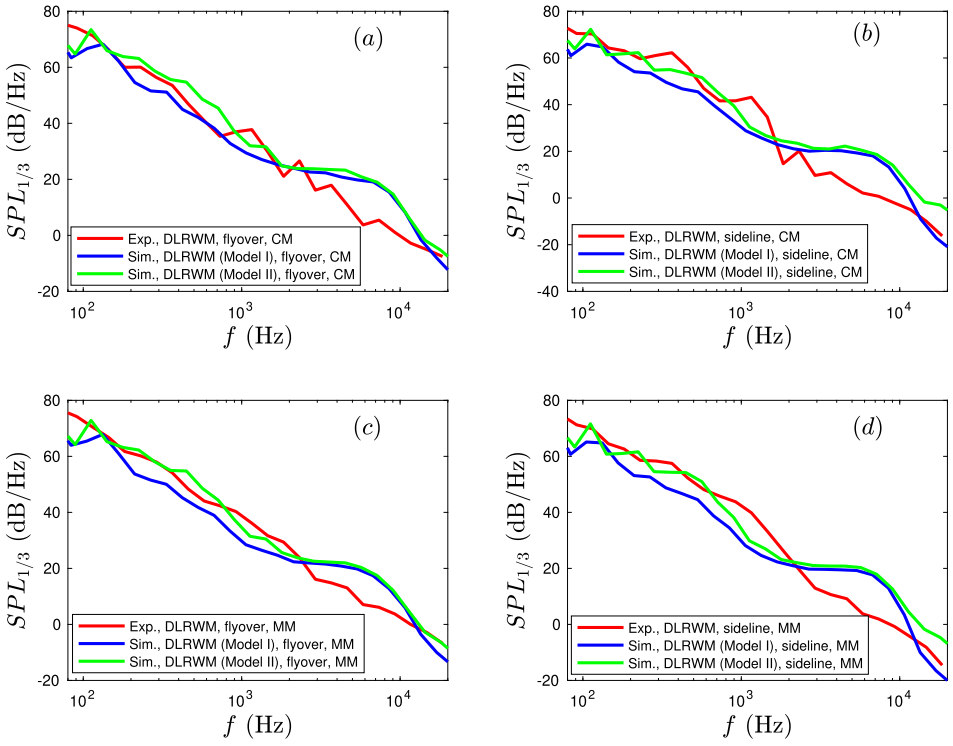

Fig. 12. The one-third octave bin-averaged sound pressure levels (SPL) of the FW-H predictions using permeable integral surfaces for the controlled case with the DLR wire-mesh fairing: (*a*) Center microphone of the flyover array; (*b*) center microphone of the sideline array; (*c*) mean of the flyover 64-microphone array; and (*d*) mean of the sideline 64-microphone array.

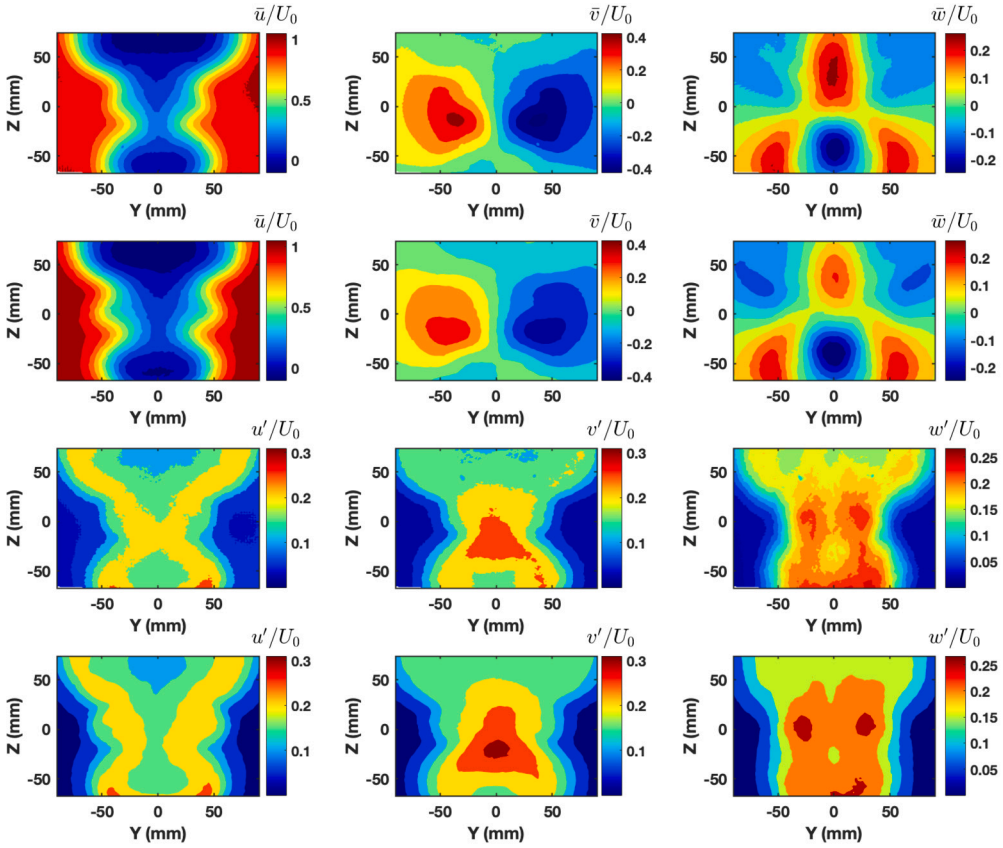

Fig. 13. Comparison of mean velocities and root-mean-square velocity fluctuations in plane $X = 170$ mm between PIV measurement and IDDES of the baseline configuration. First row: three mean velocity components of PIV; second row: three mean velocity components of IDDES; third row: root-mean-square velocity fluctuations of three velocity components of PIV; fourth row: root-mean-square velocity fluctuations of three velocity components of IDDES [53].

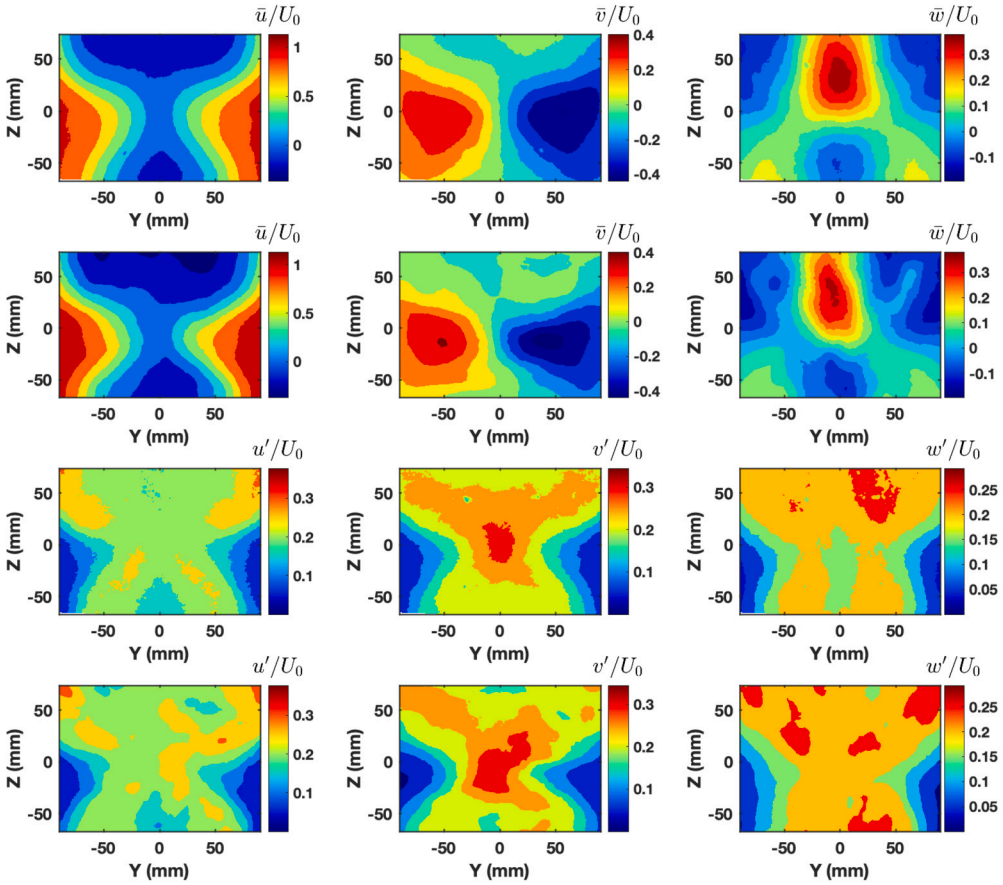

Fig. 14. Comparison of mean velocities and root-mean-square velocity fluctuations in plane $X = 170$ mm between PIV measurement and IDDES of the solid-fairing configuration. First row: three mean velocity components of PIV; second row: three mean velocity components of IDDES; third row: root-mean-square velocity fluctuations of three velocity components of PIV; fourth row: root-mean-square velocity fluctuations of three velocity components of IDDES.

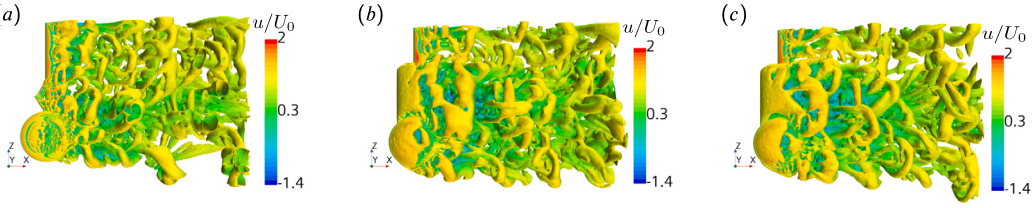

Fig. 15. Instantaneous streamwise velocity on the isosurface of $Q_{cr} = 100\ s^{-2}$ using the Q-criterion method: (*a*) Baseline case; (*b*) controlled case with a solid fairing; and (*c*) controlled case with the DLR wire-mesh fairing.

flow passes between the two wheels and accelerates at both sides of the LG rod. However, for the controlled cases, except for a small portion of airflow passing through the gaps between the fairing and the wheels, the airflow is blocked by the fairings. As a result, a wake region is formed behind the fairing upstream of the torque link and the rod. At both $Z =$ 50 and 120 mm, the wake of the controlled cases is much broader than that of the baseline case due to the shielding of the fairings. It should be noted that, at $Z = 120$ mm for the baseline case, the wake is not exactly symmetric because of the torque-link asymmetry. Overall, the contours of both controlled cases are essentially similar, demonstrating that the DLR wire mesh functions like a solid fairing.

Fig. 17 shows the pressure distribution, C_p, on the left wheel and the rod at $Z = 50$ mm. The experimental data for the controlled case with the DLR wire mesh are unavailable and therefore are not shown here. On the wheel surface, it is observed that the numerical predictions agree very well with the experiments. On the rod surface, the pressure coefficient predicted in the controlled case with a solid fairing agrees well with the experiment. However, for the baseline case, a discrepancy is observed between the numerical and experimental data on the rod surface between 80° and 120° where boundary layer separation happens [54]. Meanwhile, the numerical simulation underpredicts the pressure coefficient at $\theta > 140°$ in the rear side of the rod. Such discrepancies are possibly due to the different local Reynolds numbers between the simulation and the experiment. As a result, the boundary layer separation on the rod surface differs, so does the pressure distribution. Again, the similarity between the two controlled cases demonstrates that the DLR wire-mesh fairing functions like a solid fairing. In addition, for both controlled cases, C_p at the rod is flat, suggesting that no flow impingement takes place on the rod in the low-speed flow region behind the fairing. Thus, the fairings shield the rod and the torque link, reducing the noise generation. The shielding effect for noise reduction was also noted by Zhao et al. [13].

Fig. 18 compares the predicted flow statistics along the wake center line with PIV experiments for both the baseline and controlled cases. Overall, for both the mean streamwise velocity and the root-mean-square of the streamwise velocity fluctuation, the agreement with the ex-

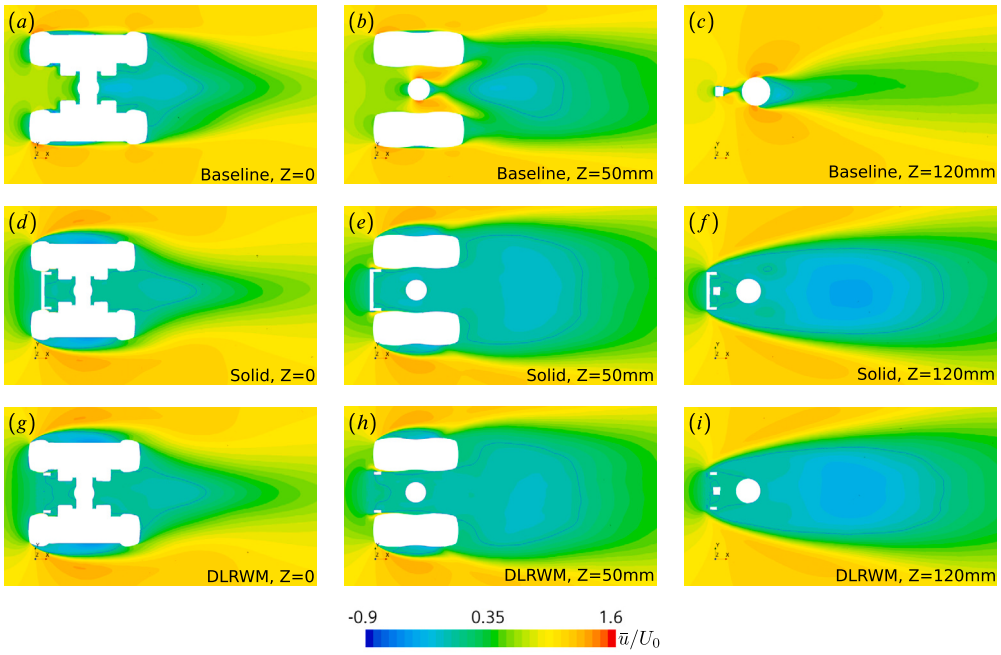

Fig. 16. Contours of the mean streamwise velocity on three different horizontal planes for the baseline and the two controlled cases. The blue lines $\bar{u} = 0$ indicate the recirculation region.

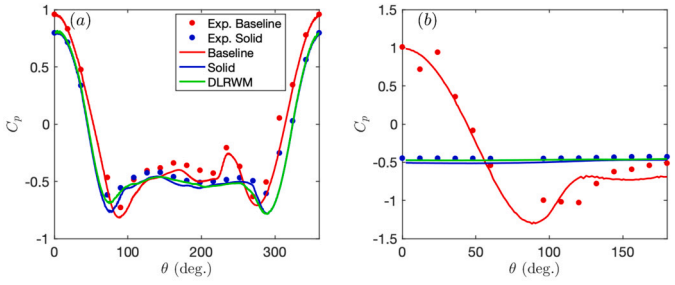

Fig. 17. Pressure coefficient on the surface of an LG wheel and a rod: (*a*) Wheel; and (*b*) rod at $Z = 50$ mm.

periments is good except at $Z = 120$ mm for the baseline case (Fig. 18(e) and (f)). For the baseline case, the discrepancy at $Z = 120$ mm between the numerical prediction and the experiment is potentially due to (i) the much finner-scale turbulence generated by the torque link which has a complex geometry with very small dimensions, and (ii) the complex joint (downstream the torque link) between the bigger and smaller rods where the grid resolution for an accurate numerical prediction becomes demanding. A much finer mesh is needed to resolve these complex geometries and small-scale turbulence. Fortunately, as will be seen in the acoustic analysis below, this does not have a significant impact on noise prediction.

Fig. 19 shows the predicted flow statistics along the vertical line at $X = 1.7d_w$ in comparison with PIV measurements. The largest discrepancy is seen, for the baseline case, at $Y = 0$ (see Fig. 19(e)), corresponding to the discrepancy shown in Fig. 18(e). As the distance from $Y = 0$ increases, the discrepancy diminishes. Overall, the agreement between the numerical simulation and the experiment is good. The agreement for the two controlled cases is generally better than that for the baseline case, suggesting that the baseline case is more challenging to simulate potentially due to the complicated turbulent wakes generated by the torque link and the complex joint (downstream the torque link) between the bigger and smaller rods, whereas these flow features are absent in the controlled cases due to the shielding of the fairings.

Table 2
Drag force of the baseline and two controlled landing gears.

Case	Baseline	Solid	DLRWM
Total Drag (N)	15	23	22
Drag of Fairing (N)	/	14	14

To compare the aerodynamic performance of the baseline and controlled configurations, Table 2 shows the drag force of the baseline and two controlled landing gears. The contribution from the solid and DLRWM fairings is the same. The total drag forces of both controlled cases are also very similar and are about 50% higher than that of the baseline case, as expected. The time-averaged pressure distribution on the solid and DLRWM fairings is shown in Fig. 20. With some noisy features of the DLRWM fairing, the pressure distribution on both fairings is very similar, again demonstrating that the DLRWM fairing functions very similarly to the solid fairing.

The sound pressure level distributed on the surface of the landing gear with and without fairings is presented in Fig. 21. Here, the sound pressure level is the logarithmic value of the ratio between the root-mean-square pressure fluctuation (p'_{rms}) and the reference pressure ($p_{ref} = 20$ μPa), as follows

$$SPL = 20 \log \left(\frac{p'_{rms}}{p_{ref}} \right). \tag{10}$$

For the baseline landing gear, the torque link and brakes are important noise sources, as demonstrated by the high-level SPL distribution on the brakes and the higher-level SPL distribution on the torque link in Fig. 21(a). With the protection from either the solid or DLR wire-mesh fairing, lower noise levels are observed on the torque link and brakes. Therefore, the fairings shield the torque link and brakes, weakening the pressure fluctuation distributed on the torque link and brakes. However, it is also observed that a noise source is shifted to the upper part of the LG rod, as shown in Fig. 21(b) and (c), because the flow is redirected due to the shielding effect of the fairings.

Fig. 22 shows the contours of the turbulent kinetic energy (TKE) on three different horizontal planes in the LG wake region for the base-

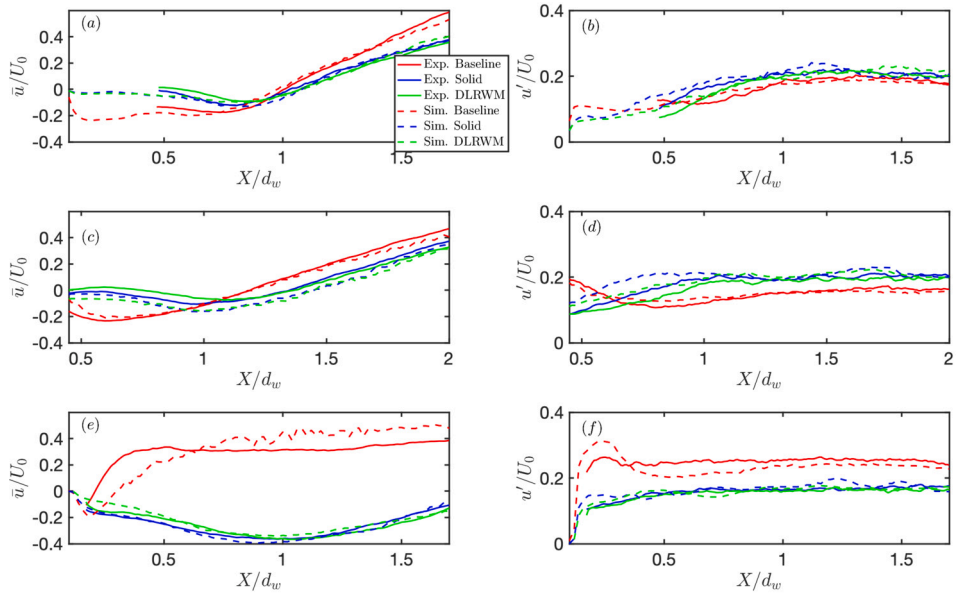

Fig. 18. Flow statistics along the wake center lines: (*a*) Mean streamwise velocity at $Z = 0$; (*b*) root-mean-square of streamwise velocity fluctuation at $Z = 0$; (*c*) mean streamwise velocity at $Z = 50$ mm; (*d*) root-mean-square of streamwise velocity fluctuation at $Z = 50$ mm; (*e*) mean streamwise velocity at $Z = 120$ mm; and (*f*) root-mean-square of streamwise velocity fluctuation at $Z = 120$ mm.

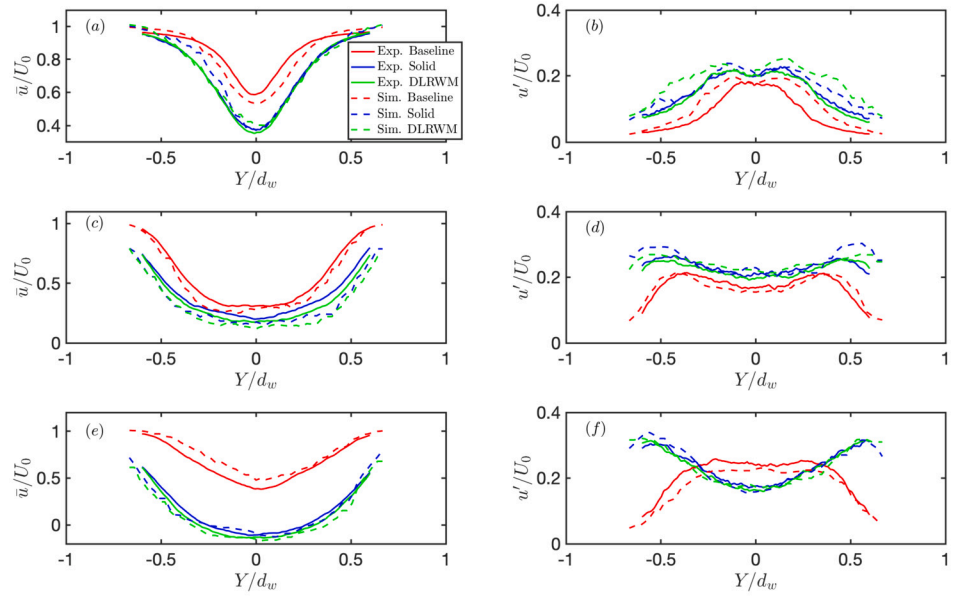

Fig. 19. Flow statistics along the wake vertical lines at $X = 1.7d_w$: (*a*) Mean streamwise velocity at $Z = 0$; (*b*) root-mean-square of streamwise velocity fluctuation at $Z = 0$; (*c*) mean streamwise velocity at $Z = 50$ mm; (*d*) root-mean-square of streamwise velocity fluctuation at $Z = 50$ mm; (*e*) mean streamwise velocity at $Z = 120$ mm; and (*f*) root-mean-square of streamwise velocity fluctuation at $Z = 120$ mm.

line and the two controlled cases. It is clear that both the solid and the DLR wire-mesh fairings broaden the turbulent wake downstream of the landing gears with generally larger values of TKE, suggesting that the fairings induce more turbulence production. This unveils the fairing-induced noise-reduction mechanism. In the presence of an add-on solid fairing or the DLR wire-mesh fairing, overall, the turbulent fluctuations are not suppressed (see also Figs. 18 and 19). However, as already seen in Fig. 16, the fairings significantly reduce the flow velocities impinging on the surfaces of the LG rod, torque link and brakes, etc, suppressing massive flow separation off these structural components. It is a reduction of impinging flow velocities, rather than a reduction of turbulence generation, that leads to the noise abatement, strengthening the summaries of bluff-body noise-reduction mechanisms using fairings by Zhao et al. [13]. It is also interesting to note that the noise-reduction mechanism here using the solid fairing and the dense DLR wire mesh is different from the mechanism using a coarse wire mesh (e.g. the ONERA wire mesh, see Fig. 2(b)) in previous studies [18–21]. The coarse ONERA wire mesh served to reduce the TKE, leading to the noise reduction of bluff bodies.

4.3. Comparison of the baseline and controlled cases: acoustic field

Fig. 23 shows the one-third octave bin-averaged SPL for both flyover and sideline configurations. Results pertaining to both the center microphones and the average of the microphone arrays are presented. Based on the numerical simulations, the FW-H analogy using a permeable in-

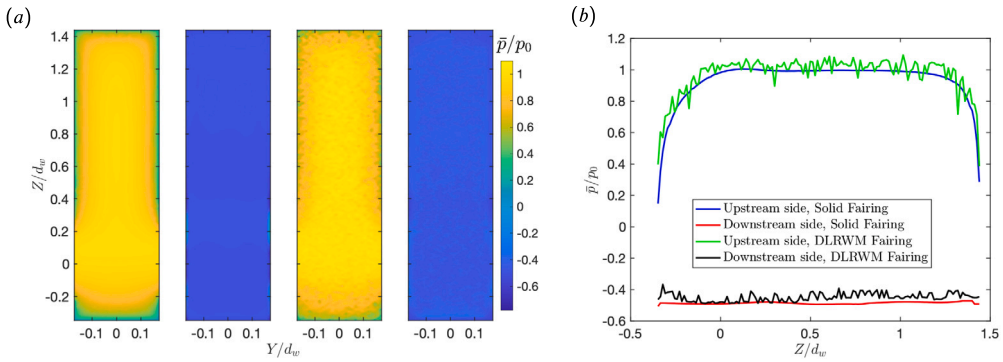

Fig. 20. Time-averaged pressure on the solid and DLRWM fairings: (*a*) From left to right: upstream side of the solid fairing, downstream side of the solid fairing, upstream side of the DLRWM fairing and downstream side of the DLRWM fairing; and (*b*) along the line Y = 0 on the upstream and downstream sides of both fairings. The dynamic pressure is $p_0 = \rho U_0^2/2$.

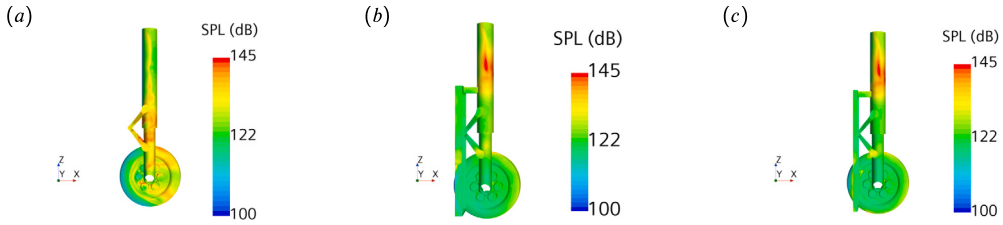

Fig. 21. Sound pressure level distributed on the surface of the landing gear: (*a*) Baseline case; (*b*) controlled case with a solid fairing; and (*c*) controlled case with the DLR wire-mesh fairing.

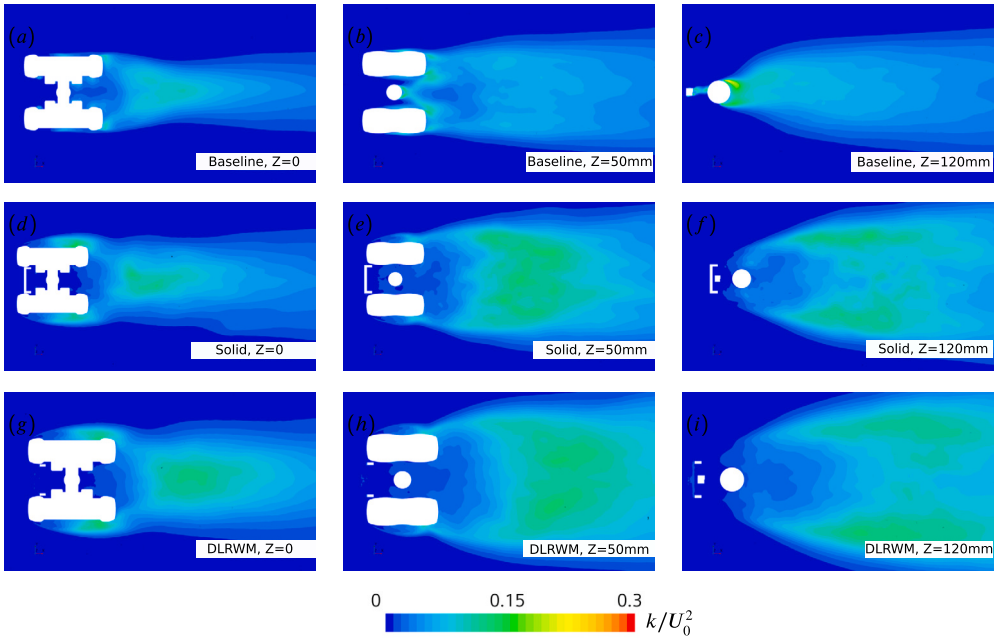

Fig. 22. Contours of the turbulent kinetic energy (k) on three different horizontal planes for the baseline and the two controlled cases.

tegral surface is adopted to predict the far-field noise. For the baseline case, the agreement between the measurements and the numerical predictions is satisfactory, particularly in the middle-frequency range. For the two controlled cases, the numerical predictions agree very well with the experiments in the low to middle frequency range but deviate from the experiments from 3000 Hz and agree with the experiment again from 12000 Hz. Given that both the spatial and temporal resolution are sufficient to resolve the noise in the above frequency range and that the baseline simulation gives a relatively good prediction in this frequency range, the reason is probably due to the small gaps between the fairings and the LG wheels, leading to insufficient accuracies in resolving the flow features in association with such gaps. It is clear that significant noise can be reduced through the introduction of a solid fairing or the porous DLR wire mesh for the landing gears. Again, for the two controlled cases, the spectra are essentially similar, indicating that the DLR wire mesh functions like a solid fairing.

Fig. 24 shows a comparison of the directivity of the SPL, defined in Eq. (10), for the three simulation cases. As compared to the baseline

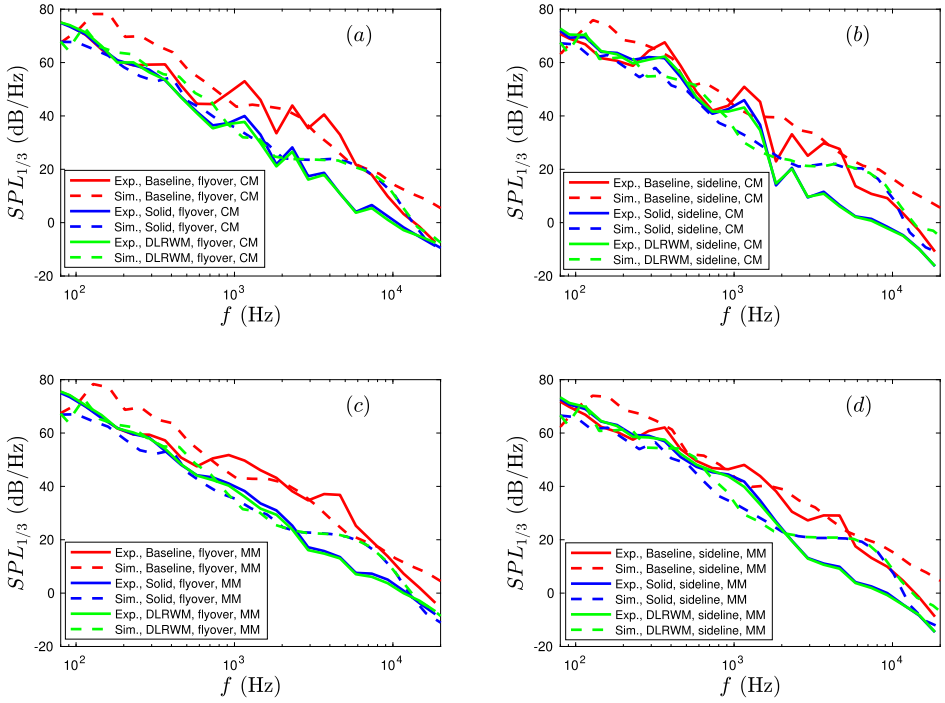

Fig. 23. The one-third octave bin-averaged SPL of the FW-H predictions: (*a*) Center microphone of the flyover array; (*b*) center microphone of the sideline array; (*c*) mean of the flyover 64-microphone array; and (*d*) mean of the sideline 64-microphone array.

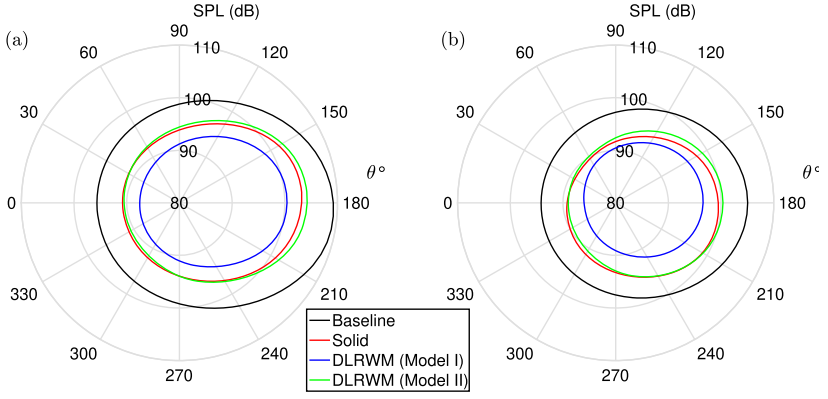

Fig. 24. Comparison of SPL directivity for the simulated baseline and controlled LAGOON landing gears: (*a*) Circle on plane $Y = 0$ with a radius of 1.05 m; and (*b*) circle on plane $Z = 0$ with a radius of 1.36 m.

case, the two controlled cases achieve a noise reduction of 4-6 dB in all radial directions. Moreover, comparing the SPL using both wire-mesh models, the directivity predicted using Model II is close to that of the controlled case with a solid fairing. However, the directivity predicted using Model I is much smaller than that of the controlled case with a solid fairing. Although no experimental data of the SPL directivity are available, the similar experimental spectra of the controlled case with a solid fairing versus those of the controlled case with the DLR wire-mesh fairing in Fig. 23 demonstrate that the noise emitted from the controlled case with a solid fairing is similar to the noise emitted from the controlled case with the DLR wire-mesh fairing. In this regard, Model II gives a much better prediction of the SPL directivity than Model I, again demonstrating the superiority of the improved wire-mesh model.

5. Concluding remarks

In this paper, we numerically and experimentally investigate the noise-reduction performance of a solid fairing and a wire-mesh fairing consisting of very fine wires and pores. The turbulent flows over a slightly modified LAGOON landing gear and two configurations, one equipped with a solid fairing and the other with a wire-mesh fairing, are simulated using IDDES. Flow and acoustic quantities in the simulations are respectively compared to the PIV and microphone measurements conducted at A-Tunnel, Delft University of Technology. An assessment of the improved wire-mesh model, recently proposed by Li et al. [33], is performed on the controlled LG with the DLR wire mesh, in comparison to the classical model [18,19]. Overall, results show that the flow and acoustic predictions given by the improved model are closer to the experiments than those given by the classical model. Thus, the improved wire-mesh model not only produces better aerodynamic predictions in internal flows (i.e. channel flows, as seen in Li et al. [33]) but also performs slightly better in both aerodynamic and aeroacoustic predictions of external flows.

For the baseline and two controlled cases, the numerically predicted pressure coefficients agree reasonably well with the experiments on both the LG wheel and rod surfaces. The predictions of the mean streamwise velocity and the root mean square of the streamwise velocity fluctuation agree reasonably well with the experimental data. It is also found

that the agreement with experiments for the two controlled cases is generally better than that for the baseline case, suggesting that the baseline case is more challenging to resolve the flow features of the freestream impingement on the torque link.

The numerically predicted and experimentally measured far-field noise, associated with the center microphones and the average of the flyover and sideline microphone configurations, are presented for the baseline case and the two controlled cases. For the baseline case, the agreement between the measurements and the numerical predictions is satisfactory, particularly in the middle-frequency range. For the two controlled cases, the numerical predictions agree very well with experiments in the low to middle frequency range but deviate from the experiments from 3000 Hz and agree with the experiment again from 12000 Hz, likely due to the challenges in resolving the flow features at the small gaps between the fairing and the LG wheels. With the aerodynamic penalty of a 50% increase in drag, the results show significant noise reduction through the installation of a solid fairing or the porous DLR wire mesh for the landing gears, owing to the fact that the fairings significantly reduce the flow velocities impinging on the surfaces of the LG rod, torque link and brakes, etc. Moreover, the directivity of the SPL shows that the two controlled cases achieve a noise reduction of 4-6 dB in all radial directions. The fairing-induced noise-reduction mechanism is also explored in this study. Both fairings effectively mitigate pressure fluctuations on the torque link and brakes, reducing surface noise sources. These findings pave the way for the low–noise design of aircraft landing gears in practical applications.

In summary, numerical wire-mesh models for representing the effects of wire meshes in flows are very useful for industrial low-noise designs supported by effective Computational Fluid Dynamics (CFD) and Computational Aero-Acoustics (CAA) analyses. The present work, exploring add-on fairings for the LG noise abatement, provides valuable insight into the noise-reduction mechanism in relation to the aerodynamic flow features manipulated by the fairings, serving practical flight testing and commercial implementation. Compared to other recent models that generate additional turbulence by altering turbulence models (e.g., Ref. [24]), the current model neither alters the SST $k-\omega$ turbulence model nor the subgrid-scale model used in the present IDDES. This is because, in the case of the dense wire-mesh fairing used here, turbulence is primarily produced by vortex shedding from the side edges of the fairing, as demonstrated by both wind-tunnel tests and numerical simulations [33,51]. Therefore, the dense DLR wire mesh functions similarly to a solid fairing, making an alteration of the turbulence model unnecessary [33]. In future work, since the present numerical model is limited to wire meshes at zero angle of incidence, it should be generalized to enable the modelling of wire meshes at any arbitrary angle of incidence. The present wire-mesh model will also probably be generalized for other porous fairings.

Funding source

This research was funded by the project Innovative Design of Installed Airframe Components for Aircraft Noise Reduction ("INVENTOR", European Union's Horizon 2020 Research and Innovation Programme) under Grant Agreement No. 8605383 and Chalmers Transport Area of Advance under Grant No. C 2023-0125-19.

CRediT authorship contribution statement

Shuai Li: Writing – original draft, Visualization, Validation, Software, Resources, Methodology, Investigation, Formal analysis, Data curation, Conceptualization. **Lars Davidson:** Writing – review & editing, Supervision, Resources, Project administration, Methodology, Investigation, Funding acquisition, Formal analysis, Conceptualization. **Shia-Hui Peng:** Writing – review & editing, Visualization, Supervision, Resources, Funding acquisition, Formal analysis. **Alejandro Rubio Carpio:** Writing – review & editing, Resources, Data curation. **Daniele Ragni:** Writing – review & editing, Resources, Data curation. **Francesco Avallone:** Writing – review & editing, Resources, Data curation. **Alexandros Koutsoukos:** Writing – review & editing, Resources, Data curation.

Declaration of competing interest

The authors declare that they have no known competing financial interests or personal relationships that could have appeared to influence the work reported in this paper.

Data availability

Data will be made available on request.

Acknowledgements

The authors would like to thank some other teams in the INVENTOR consortium who contributed to fruitful discussions during the project meetings on the modelling of porous flow-through fairings, i.e. the Office National d'Études et de Recherches Aérospatiales (ONERA) and RWTH Aachen University. The authors would also like to thank other teams who contributed to the definition, manufacturing and tests of the fairings, i.e. Dassault Aviation, the German Aerospace Center, the ONERA and the von Karman Institute for Fluid Dynamics, etc. Dr. Muye Ge in the Division of Marine Technology at Chalmers is gratefully acknowledged for helpful discussions on some technical issues on the simulation of landing gears. The computations were enabled by resources provided by the Swedish National Infrastructure for Computing (SNIC) partially funded by the Swedish Research Council through grant agreement no. 2018-05973.

Appendix A

The FW-H equation in its standard differential reads [37,42]

$$\Box^2 p'(\mathbf{x},t) = \frac{\partial}{\partial t}\left[\left(\rho_0 U_n\right)\delta(f)\right] - \frac{\partial}{\partial x_i}\left[L_i\delta(f)\right] + \frac{\partial^2}{\partial x_i \partial x_j}\left[T_{ij}H(f)\right], \tag{11}$$

where $\Box^2$, equivalent to $\left(1/c^2\right)\left(\partial^2/\partial t^2\right) - \nabla^2$, represents the D'Alembertian operator. ρ_0 is the density of far-field undisturbed medium. $H(f)$ and $\delta(f)$ are the Heaviside function and the Dirac delta function, respectively. U_n, L_i and the Lighthill stress tensor T_{ij} are defined, respectively, as

$$U_n = \left(1 - \frac{\rho}{\rho_0}\right) v_n + \frac{\rho u_n}{\rho_0}, \tag{12}$$

$$L_i = P_{ij} n_j + \rho u_i \left(u_n - v_n\right), \tag{13}$$

$$T_{ij} = \rho u_i u_j + \left[\left(p - p_0\right) - \left(\rho - \rho_0\right) c^2\right]\delta_{ij} - \sigma_{ij}, \tag{14}$$

where v_n is the surface velocity component normal to the surface, u_n is the fluid velocity component normal to the surface, n_j is the surface normal vector, u_i is the fluid velocity component in the i direction, p_0 is the pressure of far-field undisturbed medium, c is the sound speed, δ_{ij} is the Kronecker delta, and σ_{ij} is the viscous stress tensor. P_{ij} is the compressive stress tensor and is expressed as

$$P_{ij} = \left(p - p_0\right)\delta_{ij} - \sigma_{ij}. \tag{15}$$

Using Farassat's formulation 1A [40,41], an integral representation of the solution of Eq. (11) can be expressed as

$$p'(\mathbf{x},t) = p'_T(\mathbf{x},t) + p'_L(\mathbf{x},t) + p'_Q(\mathbf{x},t), \tag{16}$$

where $p'_T(\mathbf{x},t)$, $p'_L(\mathbf{x},t)$ and $p'_Q(\mathbf{x},t)$ represent the monopole (thickness), dipole (loading) and quadrupole terms, respectively. $p'_T(\mathbf{x},t)$ and $p'_L(\mathbf{x},t)$ can be respectively expressed as

$$p'_T(\mathbf{x},t) = \frac{1}{4\pi}\int_{f=0}\left[\frac{\rho_0\left(\dot{U}_n + U_{\dot{n}}\right)}{r\left(1-M_r\right)^2}\right]_{ret} dS + \frac{1}{4\pi}\int_{f=0}\left[\frac{\rho_0 U_n\left[r\dot{M}_r + c\left(M_r - M^2\right)\right]}{r^2\left(1-M_r\right)^3}\right]_{ret} dS, \tag{17}$$

$$p'_L(\mathbf{x},t) = \frac{1}{4\pi c}\int_{f=0}\left[\frac{\dot{L}_r}{r\left(1-M_r\right)^2}\right]_{ret} dS + \frac{1}{4\pi}\int_{f=0}\left[\frac{L_r - L_M}{r^2\left(1-M_r\right)^2}\right]_{ret} dS + \frac{1}{4\pi c}\int_{f=0}\left[\frac{L_r\left[r\dot{M}_r + c\left(M_r - M^2\right)\right]}{r^2\left(1-M_r\right)^3}\right]_{ret} dS, \tag{18}$$

in which $r = |\mathbf{x} - \mathbf{y}|$ is the distance between observer and source, $f = 0$ represents the integral surface, and $M = |\mathbf{M}|$ where $\mathbf{M}$ is the local Mach number vector of source with respect to a frame fixed to the undisturbed medium [55]. A dot over a variable implies the derivative with respect to source time of that variable. A subscript r or n indicates a dot product of the vector with the unit vector in the radiation direction $\mathbf{r}$ or the unit vector in the surface normal direction $\mathbf{n}$, respectively. Namely, $U_n = U_i n_i$, $U_{\dot{n}} = U_i \dot{n}_i$, $M_r = M_i r_i$, $L_r = L_i r_i$, $L_M = L_i M_i$, and $M_i = v_i/c$ where v_i represents the surface velocity component in the i direction. The subscript *ret* indicates quantities evaluated at the retarded time $\tau = t - r/c$.

It should be noted that, for an impermeable integral surface, the surface velocity component normal to the surface is equal to the fluid velocity component normal to the surface, i.e. $u_n = v_n$. At low Mach numbers, the quadrupole contribution $p'_Q(\mathbf{x},t)$ is very small and can be neglected. For a permeable integral surface, the integral surface is expected to enclose all quadrupole sources. The permeable FW-H formulation assumes that the contribution to the total noise of volumetric sources outside the integral surface is negligible [38,56].

References

[1] D.A. Black, J.A. Black, T. Issarayangyun, S.E. Samuels, Aircraft noise exposure and resident's stress and hypertension: A public health perspective for airport environmental management, J. Air Transp. Manag. 13 (5) (2007) 264–276.

[2] R.N. Lawton, D. Fujiwara, Living with aircraft noise: Airport proximity, aviation noise and subjective wellbeing in England, Transp. Res., Part D, Transp. Environ. 42 (2016) 104–118.

[3] M. Choudhari, D. Lockard, Simulations & measurements of airframe noise: A banc workshops perspective, in: Specialists Meeting on "Progress and Challenges in Validation Testing for Computational Fluid Dynamics" (AVT-246), 2016, no. NF1676L-23007.

[4] W. Dobrzynski, M. Pott-Pollenske, D. Foot, M. Goodwin, Landing gears aerodynamic interaction noise, in: Proceedings of European Congress on Computational Methods in Applied Sciences and Engineering (ECCOMAS), 2004.

[5] W. Liu, J.W. Kim, X. Zhang, D. Angland, B. Caruelle, Landing-gear noise prediction using high-order finite difference schemes, J. Sound Vib. 332 (14) (2013) 3517–3534.

[6] W. Dobrzynski, R. Ewert, M. Pott-Pollenske, M. Herr, J. Delfs, Research at DLR towards airframe noise prediction and reduction, Aerosp. Sci. Technol. 12 (1) (2008) 80–90.

[7] W. Dobrzynski, L. Chow, P. Guion, D. Shiells, Research into landing gear airframe noise reduction, in: 8th AIAA/CEAS Aeroacoustics Conference & Exhibit, 2002, p. 2409.

[8] W.M. Dobrzynski, B. Schöning, L.C. Chow, C. Wood, M. Smith, C. Seror, Design and testing of low noise landing gears, Int. J. Aeroacoust. 5 (3) (2006) 233–262.

[9] W. Dobrzynski, L.C. Chow, M. Smith, A. Boillot, O. Dereure, N. Molin, Experimental assessment of low noise landing gear component design, Int. J. Aeroacoust. 9 (6) (2010) 763–786.

[10] A. Abeysinghe, J. Whitmire, D. Nesthus, J. Moe, G. Stuczynski, QTD 2 (Quiet Technology Demonstrator 2) main landing gear noise reduction fairing design and analysis, in: 13th AIAA/CEAS Aeroacoustics Conference (28th AIAA Aeroacoustics Conference), 2007, p. 3456.

[11] J. Kennedy, E. Neri, G.J. Bennett, The reduction of main landing gear noise, in: 22nd AIAA/CEAS Aeroacoustics Conference, 2016, p. 2900.

[12] R. Merino-Martínez, J. Kennedy, G.J. Bennett, Experimental study of realistic low–noise technologies applied to a full–scale nose landing gear, Aerosp. Sci. Technol. 113 (2021) 106705.

[13] K. Zhao, P. Okolo, E. Neri, P. Chen, J. Kennedy, G.J. Bennett, Noise reduction technologies for aircraft landing gear-A bibliographic review, Prog. Aerosp. Sci. 112 (2020) 100589.

[14] S. Oerlemans, C. Sandu, N. Molin, J.-F. Piet, Reduction of landing gear noise using meshes, in: 16th AIAA/CEAS Aeroacoustics Conference, 2010, p. 3972.

[15] M. Smith, L. Chow, N. Molin, Control of landing gear noise using meshes, in: 16th AIAA/CEAS Aeroacoustics Conference, 2010, p. 3974.

[16] P.N. Okolo, K. Zhao, J. Kennedy, G.J. Bennett, Mesh screen application for noise reduction of landing gear strut, in: 22nd AIAA/CEAS Aeroacoustics Conference, 2016, p. 2845.

[17] P.N. Okolo, K. Zhao, J. Kennedy, G.J. Bennett, Numerical modeling of wire screens for flow and noise control, in: 23rd AIAA/CEAS Aeroacoustics Conference, 2017, p. 3700.

[18] W. Zhu, Z. Xiao, S. Fu, Simulations of turbulence screens for flow and noise control in tandem cylinders, Red 105 (2019) 1.

[19] W. Zhu, Z. Xiao, S. Fu, Numerical modeling screen for flow and noise control around tandem cylinders, AIAA J. 58 (6) (2020) 2504–2516.

[20] M. Terracol, E. Manoha, Development of a wire mesh screen model for unsteady simulation of noise reduction devices, with application to the tandem cylinder configuration, in: 2018 AIAA/CEAS Aeroacoustics Conference, 2018, p. 3473.

[21] M. Terracol, E. Manoha, Numerical wire mesh model for the simulation of noise-reduction devices, AIAA J. 59 (3) (2021) 987–1007.

[22] M. Gondrum, A. Niemöller, M. Meinke, W. Schroeder, A. Rubio Carpio, D. Ragni, F. Avallone, Landing gear noise mitigation by an upstream installed fairing, in: 28th AIAA/CEAS Aeroacoustics 2022 Conference, 2022, p. 2847.

[23] G.J. Bennett, J. Lai, G. O'Brien, D. Ragni, F. Avallone, M. Pott-Pollenske, Flow control and passive low noise technologies for landing gear noise reduction, in: 28th AIAA/CEAS Aeroacoustics 2022 Conference, 2022, p. 2848.

[24] M. Terracol, E. Manoha, L. Manueco, F. Avallone, D. Ragni, A. Rubio Carpo, Numerical simulations of a landing gear with flow through fairings for noise mitigation, in: AIAA AVIATION 2023 Forum, 2023, p. 4173.

[25] D. Casalino, A.F. Ribeiro, E. Fares, S. Nölting, Lattice–Boltzmann aeroacoustic analysis of the LAGOON landing-gear configuration, AIAA J. 52 (6) (2014) 1232–1248.

[26] E. Manoha, B. Caruelle, Summary of the LAGOON solutions from the benchmark problems for airframe noise computations-III workshop, in: 21st AIAA/CEAS Aeroacoustics Conference, 2015, p. 2846.

[27] L. Sanders, E. Manoha, S. Ben Khelil, C. Francois, LAGOON: new mach landing gear noise computation and further analysis of the CAA process, in: 18th AIAA/CEAS Aeroacoustics Conference (33rd AIAA Aeroacoustics Conference), 2012, p. 2281.

[28] J.-C. Giret, A. Sengissen, S. Moreau, J.-C. Jouhaud, Prediction of LAGOON landing-gear noise using an unstructured LES solver, in: 19th AIAA/CEAS Aeroacoustics Conference, 2013, p. 2113.

[29] D. Casalino, A.F. Ribeiro, E. Fares, Facing rim cavities fluctuation modes, J. Sound Vib. 333 (13) (2014) 2812–2830.

[30] F. de la Puente, L. Sanders, F. Vuillot, On LAGOON nose landing gear CFD/CAA computation over unstructured mesh using a ZDES approach, in: 20th AIAA/CEAS Aeroacoustics Conference, 2014, p. 2763.

[31] A. Sengissen, J.-C. Giret, C. Coreixas, J.-F. Boussuge, Simulations of LAGOON landing-gear noise using lattice Boltzmann solver, in: 21st AIAA/CEAS Aeroacoustics Conference, 2015, p. 2993.

[32] T.R. Ricciardi, W.R. Wolf, R. Speth, Acoustic prediction of LAGOON landing gear: cavity noise and coherent structures, AIAA J. 56 (11) (2018) 4379–4399.

[33] S. Li, L. Davidson, S.-H. Peng, Numerical modeling of a wire mesh for aerodynamic noise reduction, Phys. Fluids 35 (1) (2023) 015103.

[34] R. Merino-Martínez, A.R. Carpio, L.T.L. Pereira, S. van Herk, F. Avallone, D. Ragni, M. Kotsonis, Aeroacoustic design and characterization of the 3D-printed, open-jet, anechoic wind tunnel of Delft University of Technology, Appl. Acoust. 170 (2020) 107504.

[35] P. Welch, The use of fast Fourier transform for the estimation of power spectra: A method based on time averaging over short, modified periodograms, IEEE Trans. Audio Electroacoust. 15 (2) (1967) 70–73.

[36] M. Gondrum, M. Meinke, W. Schroeder, F. Avallone, D. Ragni, Porous fairings for landing gear noise mitigation, in: 30th AIAA/CEAS Aeroacoustics Conference (2024), 2024, p. 3174.

[37] Siemens Digital Industries Software, Simcenter STAR-CCM+, version 2021.1, Siemens, 2021.

[38] Siemens Digital Industries Software, Simcenter STAR-CCM+ User Guide v. 2021.1, Siemens, 2021.

[39] M.S. Gritskevich, A.V. Garbaruk, J. Schütze, F.R. Menter, Development of DDES and IDDES formulations for the k-ω shear stress transport model, Flow Turbul. Combust. 88 (3) (2012) 431–449.

[40] F. Farassat, G.P. Succi, The prediction of helicopter rotor discrete frequency noise, in: American Helicopter Society, 1982, pp. 497–507.

[41] K.S. Brentner, Prediction of helicopter rotor discrete frequency noise: A computer program incorporating realistic blade motions and advanced acoustic formulation, Tech. rep., 1986.

[42] K.S. Brentner, F. Farassat, Analytical comparison of the acoustic analogy and Kirchhoff formulation for moving surfaces, AIAA J. 36 (8) (1998) 1379–1386.

[43] C. Teruna, F.A. Manegar, F. Avallone, D. Casalino, D. Ragni, A. Rubio Carpio, T. Carolus, Numerical analysis of metal-foam application for trailing edge noise reduction, in: 25th AIAA/CEAS Aeroacoustics Conference, 2019, p. 2650.
[44] C. Teruna, F. Manegar, F. Avallone, D. Ragni, D. Casalino, T. Carolus, Noise reduction mechanisms of an open-cell metal-foam trailing edge, J. Fluid Mech. 898 (2020).
[45] C. Teruna, L. Rego, F. Avallone, D. Ragni, D. Casalino, Applications of the multi-layer porous medium modeling approach for noise mitigation, J. Aerosp. Eng. 34 (6) (2021) 04021074.
[46] S. Li, L. Davidson, S.-H. Peng, A pressure-loss model for flow-through round-hole perforated plates of moderate porosity and thickness in laminar and turbulent flow regimes, Int. J. Heat Mass Transf. 226 (2024) 125490.
[47] T. Kurian, J.H. Fransson, Grid-generated turbulence revisited, Fluid Dyn. Res. 41 (2) (2009) 021403.
[48] A.R. Carpio, F. Avallone, D. Ragni, On the role of the flow permeability of metal foams on trailing edge noise reduction, in: 2018 AIAA/CEAS Aeroacoustics Conference, 2018, p. 2964.
[49] A.R. Carpio, R.M. Martínez, F. Avallone, D. Ragni, M. Snellen, S. van der Zwaag, Experimental characterization of the turbulent boundary layer over a porous trailing edge for noise abatement, J. Sound Vib. 443 (2019) 537–558.
[50] A.R. Carpio, F. Avallone, D. Ragni, M. Snellen, S. van der Zwaag, Quantitative criteria to design optimal permeable trailing edges for noise abatement, J. Sound Vib. 485 (2020) 115596.
[51] E. Gallo, R. Zamponi, A. Zarri, Y.C. Kucukosman, C.F. Schram, Experimental characterization of flow through porous fairings, in: AIAA AVIATION 2023 Forum, 2023, p. 4175.
[52] F. Méry, D. Sebbane, Aerodynamic characterisation of porous fairings: pressure drop and laser Doppler velocimetry measurements, Sci. Data 10 (1) (2023) 39.
[53] S. Li, L. Davidson, S.-H. Peng, A. Rubio Carpio, D. Ragni, F. Avallone, Numerical and experimental investigation of the mitigation of landing gear noise using diamond lattice fairings, in: 30th AIAA/CEAS Aeroacoustics Conference (2024), 2024, p. 3283.
[54] S. Li, D.E. Rival, X. Wu, Sound source and pseudo-sound in the near field of a circular cylinder in subsonic conditions, J. Fluid Mech. 919 (2021) A43.
[55] K.S. Brentner, F. Farassat, Modeling aerodynamically generated sound of helicopter rotors, Prog. Aerosp. Sci. 39 (2–3) (2003) 83–120.
[56] M. Ge, Numerical prediction of propeller induced hull pressure pulses and noise, Chalmers Tekniska Högskola, Sweden, 2021.